Palaeogeography, Palaeoclimatology, Palaeoecology
April 2022, Volume 568, Pages 110280 (14p.)
https://doi.org/10.1016/j.palaeo.2021.110280
https://archimer.ifremer.fr/doc/00679/79102/

Monitoring Australian Monsoon variability over the past four glacial cycles

Pei Renjie [1, *], Kuhnt Wolfgang [1], Holbourn Ann [1], Hingst Johanna [1, 2], Koppe Matthias [1], Schultz Jan [1], Kopetz Peer [1], Zhang Peng [3], Andersen Nils [4]

[1] Institute for Geosciences, Kiel University, Ludewig-Meyn Str. 10-14, 24118 Kiel, Germany
[2] MARUM, University of Bremen University, Leobener Str. 8, 28359 Bremen, Germany
[3] State Key Laboratory of Continental Dynamics, Department of Geology, Northwest University, Xi'an 710069, China
[4] Leibniz Laboratory for Radiometric Dating and Stable Isotope Research, Kiel University, Max-Eyth-Str. 11-13, 24118 Kiel, Germany

* Corresponding author : Renjie Pei, email address : Renjie.Pei@ifg.uni-kiel.de

Wolfgang.kuhnt@ifg.uni-kiel.de ; Ann.Holbourn@ifg.uni-kiel.de ; jhingst@marum.de ; stu121922@mail.uni-kiel.de ; nandersen@leibniz.uni-kiel.de

Abstract :

We analyse changes in terrigenous sedimentation along the northwestern Australian margin to monitor the latitudinal migration of the Intertropical Convergence Zone (ITCZ) and the shifting boundaries of climatic belts during the last four glacial cycles. We integrate high-resolution X-ray fluorescence (XRF) scanning elemental records from Core SO257–18548 and International Ocean Discovery Program Site U1482, situated southwest of the Scott Plateau at the southern edge of the present-day monsoonal belt, and from Core SO257–18571, located within the dust-cyclone belt offshore Northwest Cape south of the Exmouth Plateau. The chronology of these sediment successions is based on 14C dating over the last glacial termination and on correlation of the benthic oxygen isotope record to the LR04 stack (Lisiecki and Raymo, 200) and Antarctic ice core chronology. Our XRF derived records of riverine terrigenous run-off and aeolian dust input reveal rapid intensification of monsoonal precipitation and reduction of atmospheric dust during the Younger Dryas and early Holocene as well as during the terminal phase of other major deglaciations. Short-lived monsoonal maxima in the early Holocene (~10 ka), MIS 5e (~130 ka), MIS 7 (~200, ~220 and ~ 240 ka), and MIS 9 (~280, ~305 and ~ 330 ka) coincide with maxima in atmospheric carbon dioxide and methane concentrations. Monsoon intensification occurs during maxima in Southern Hemisphere spring (September) insolation, when intense heat low pressure cells over the Pilbara region trigger the southward shift of the ITCZ. Within the dust-cyclone belt, riverine sediment discharge was restricted to intervals of high atmospheric CO2 concentrations, when sea surface temperature thresholds promoted cyclone formation in the tropical Indian Ocean. Northwestern Australia remained dry and arid during MIS 5a-d, when the ITCZ was locked in a more northerly position and temperature thresholds were not attained.

Highlights

► Rapid intensification of Australian monsoon at end of glacial terminations I to IV ► Monsoon intensification coincided with atmospheric CO_2 increase ► Austral spring insolation drove southward shift of ITCZ and monsoon intensification ► Formation of regional heat lows instrumental for monsoonal hydroclimate ► Aeolian dust dominant during glacials and MIS 5a-d south of 20°S.

Keywords : ITCZ, Glacial terminations, Dust, Terrigenous discharge, Oxygen isotopes, X-Ray fluorescence

1. Introduction

The climate and hydrography of the eastern Indian Ocean (Timor Sea) and northwestern Australia are strongly influenced by seasonal changes in wind direction associated with the southward migration of the Intertropical Convergence Zone (ITCZ) during austral summer. During December-February, NW winds predominate and rainfall increases over Indonesia and northern Australia (Australian summer monsoon), whereas dry SE Trade Winds prevail during austral winter (June-November). Today, a striking feature of northwestern Australian climate is the formation of low pressure cells between September and November, which precede the monsoon season by up to three months. The development of these heat lows is a critical factor in the formation of the Australian summer monsoon circulation, as they trigger strong westerly winds (Suppiah, 1992). These heat lows form over the desert regions under clear skies at high insolation in areas were surface albedo is high. The intensity and geographic extent of these heat lows are highly sensitive to changes in insolation, thus responding to both external insolation and internal greenhouse forcing.

On longer timescales, variations in monsoonal rainfall are related to changes in precessional summer insolation, sea level fluctuations and atmospheric CO_2 concentrations (e.g., Wyrwoll et al., 2007; Griffiths et al., 2009; DiNezio and Tierney, 2013; Kuhnt et al., 2015). There is also a broad consensus that the meridional position of the ITCZ, which controls the latitudinal extent of monsoonal rainfall, is strongly dependent on the interhemispheric temperature gradient (e.g., Schneider et al., 2014; Mohtadi et al., 2016). Climate models predict drier subtropics in the Southern Hemisphere during interstadials due to a northward shift of the ITCZ during Dansgaard-Oeschger (D/O) warming events in the Northern Hemisphere and a southward displacement of the ITCZ during Northern Hemisphere cooling (Claussen et al., 2003; Broccoli et al., 2006; Chiang et al., 2008). These changes likely result from shifts in the atmospheric heat exchange between the tropics and mid latitudes and attendant variations in Trade Winds (e.g., Broccoli et al., 2006). However, the response of the Australian Monsoon to high-latitude temperature fluctuations on orbital, suborbital and millennial timescales is still poorly understood due to the scarcity of continuous high-resolution precipitation and runoff records from the Australian continent.

The sedimentary archives along the northwestern Australian margin, south of the fulcrum of the ITCZ's seesaw, are ideally situated to test the validity of these model predictions. The seasonal southward and northward migrations of the ITCZ and associated austral monsoonal rain belt directly influence sedimentation patterns in the Timor Sea. Austral summer monsoon rainfall during southward shifts of the ITCZ increases river discharge, leading to enhanced deposition of terrigenous sediment along the continental margin. In contrast, when the ITCZ is locked into a more northerly position, the austral summer monsoon weakens, vast areas of northern Australia dry out and intensified Trade Winds in austral winter carry increased amounts of dust from the arid zones of central and northwestern Australia into the SE Timor Sea. Sedimentation patterns along the northwestern Australian margin are, thus, directly related

to the latitudinal migration of the monsoon rain belt, making this area ideally suited to test model predictions of Southern (Northern) Hemisphere temperature forcing of the Australian Monsoon.

Today, the delivery of dust from the Australian continent towards the eastern Indian Ocean is controlled by the seasonal change in wind direction associated with the southward migration of the ITCZ during austral summer. During December-February, NW winds predominate and rainfall increases over Indonesia and northern Australia (Australian summer monsoon), whereas dry SE Trade Winds, which transport dust particles originating from the central Australian deserts, prevail during austral winter-spring in June-October. Pioneering sedimentologic studies of sediment cores offshore northwestern Australia suggested that changes in grain size offer a valuable proxy to estimate the amount of wind-blown desert dust in the terrigenous fraction of hemipelagic sediments in this area (Heirtzler 1974; Mc Tainsh, 1989; Hesse and McTainsh, 2003). Furthermore, these studies provided evidence that provenance and transport mechanisms (wind direction and intensity) were highly variable over orbital timescales. For example, grain size analysis in Core SO14-08-05 (16° 21' S, 118° 23' E) on the Rowley Terrace between the Scott Plateau and Exmouth Plateau indicated that the dust flux consisted of coarser grains during the Last Glacial Maximum (LGM) in comparison to the early Holocene (Turney et al., 2006). This record also exhibits maxima in dust flux at ~8, 14, 30 and 150 ka (MIS 6), associated with Southern Hemisphere cooler climate phases (Hesse and McTainsh, 2003, Hesse et al., 2004; Turney et al, 2006). Spikes of aeolian quartz grains in Lake Carpentaria also coincide with Northern Hemisphere warm phases/Southern Hemisphere cool phases (De Deckker, 2001), in particular dust peaks centered at 24.0, 25.4 and 29.5 ka and two peaks within broader maxima at ~34.6 and ~38.6 ka are associated with D/O-Events 3, 4, 7 and 8.

Previous studies of Australian sedimentary archives also suggested that the northern Australian monsoonal rainbelt expanded and intensified during suborbital cooling and drying phases in the Northern Hemisphere. The Lynch's Crater sediment records provided evidence for intensified monsoonal rainfall over northern Australia during Heinrich 1-3 stadials (HS 1-3) and the Holocene 8.2 ka cold event (Muller et al., 2008). By contrast, Northern Hemisphere tropical and equatorial rainfall was weakest during these cold phases. In records from the SE Asian Maritime Continent, such as northern Borneo (Partin et al., 2007), the Sulu Sea (Rosenthal et al, 2003) and Sulawesi (Schröder et al., 2016, 2018), the weakest tropical convection and driest conditions characterize the early deglaciation HS 1 (18-15 ka). While there is evidence of a suborbital seesaw in monsoonal rainfall intensity for the LGM, deglaciation and early Holocene, the long-term orbital and suborbital evolution of the Australian Monsoon remains enigmatic, mainly due to the scarcity of continuous high-resolution records extending beyond the last glacial cycle. The only high-resolution monsoonal records that cover this extended time interval are located further to the northeast and are strongly influenced by upwelling-related productivity changes of the Indonesian Throughflow, driven by monsoonal winds during glacial low stands (Holbourn et al., 2005; Kawamura et al., 2006; Sarnthein et al., 2011). IMAGES Core MD00-2361, located at the margin of the Exmouth Plateau near the North West Cape, tracked glacial-interglacial changes in riverine and dust supply over the last 550 kyr, but the relatively low mean sedimentation rates of 2.5 cm/kyr with substantially lower rates

during glacials did not allow full reconstruction of millennial scale monsoonal variability at this location (Stuut et al., 2014).

Here, we compare X-ray fluorescence (XRF) core scanner-derived elemental records in two extended sediment successions retrieved at the southern edge of the present-day monsoonal belt southwest of the Scott Plateau and within the dust-cyclone belt offshore Northwest Cape to monitor monsoonal runoff and dust fluxes on millennial timescales over the last four glacial cycles. Our main objectives are to reconstruct the variability of the tropical convection along the southernmost displacement of the ITCZ during austral summer in relation to changes in high-latitude climate, sea level and atmospheric greenhouse gas concentration in order to monitor changes in the latitudinal temperature gradient and the intensity of the Walker circulation.

2. Regional setting

2.1 *Climate archives along the northwestern Australian margin*

Deep-water sediments along the northwestern Australian margin consist of autochthonous biogenic carbonate with a small biosiliceous component and fine-grained terrigenous input from the Australian continent, which bypasses the broad shelf in suspension. One of the most prominent features is a distinct NE-SW decrease in late Pleistocene-Holocene sedimentation rates (Keep et al., 2018; Kuhnt et al., 2018). This trend has been explained by a combination of southward decreasing subsidence and accommodation space with increasing distance from the northern margin of the Australian plate (Keep et al., 2018) and decreasing discharge of riverine sediment southward of the Australian monsoonal rain belt (Gingele and De Deckker 2004; De Deckker et al., 2014; Kuhnt et al., 2015). R/V Sonne Cruise 257 (WACHEIO) retrieved a suite of sediment cores along transects seaward of the northwestern Australian shelf to better understand the sediment transport offshore and the dynamics of depositional systems and to reconstruct long-term climate evolution from these high-resolution sediment archives. Preliminary evaluation indicates that sedimentation rates exceeded 5 cm/kyr during the late Pleistocene to Holocene in the northeastern part of the margin, whereas the Rowley Terrace between the Scott Plateau and Exmouth Plateau displays intermediate sedimentation rates ranging between 2.8 and 5.0 cm/kyr (Figure 1). South of the Exmouth Peninsula, sedimentation rates are generally below 2 cm/kyr and increase basinwards, which highlights the important role of slope-parallel sediment advection in this area (Figure 1).

2.2 *Factors influencing fluvial sediment discharge*

The amount and chemical composition of sediment discharge by rivers from the Australian continent are influenced by multiple factors including the catchment-basin size, the relief and associated stream gradient, the bedrock lithology, the tectonic setting, and ultimately the amount and seasonality of rainfall. The succession of climate belts in northwestern Australia from (1) monsoonal tropical humid in the north through (2) tropical semi-arid with sporadic rainfall from cyclones during the summer monsoon

season, (3) arid and (4) temperate with dominant rain in austral winter in the south (Figure 1) is reflected in the composition of the river sediment loads and marine surface sediments along the adjacent margin. However, clay mineral distribution offshore northwestern Australia does not exhibit a simple latitudinal distribution pattern, with kaolinite (Al-Fe rich) dominating in warm and humid latitudes and illite/chlorite (K-rich) in cold and arid regions (Gingele et al., 2001). High illite and chlorite concentrations also occur near the equator and high kaolinite concentrations were observed south of 35°, which has been attributed to specific local sources (Gingele et al. 2001; Gingele and DeDeckker, 2004). These authors found illite concentrations of 25-36 % in rivers discharging from the monsoonal climate zone in northern Australia with particularly high illite concentrations (50 and 54 % of the clay mineral content) in sediments from the Ashburton River and adjacent Mangrove Creek, which discharge from the semi-arid Pilbara mountain range. These results are consistent with potassium (K) concentrations in chemical analyses of sediments from these rivers and adjacent offshore regions (Figure 2). A possible explanation for the high illite content in clay mineral assemblages and the associated high K concentrations in the elemental composition of the fine grained sediment from the semi-arid zone is the intense erosion in elevated parts of the catchment during catastrophic rainfall events and the rapid and direct sediment transport in sporadic flash floods.

3. Material and methods

3.1. Core locations and sediment recovery

Piston Core SO257-18548 (15°3.59’S, 120°18.846’ E, 1608.2 m water depth, 11.2 m core length) and International Ocean Discovery Program (IODP) Site U1482 (15°3.32′S, 120°26.10′E, 1466 m water depth), located close to the modern southern limit of the seasonal (austral summer) displacement of the ITCZ, are influenced by the monsoonal discharge from the nearby Fitzroy River (Figure 2). Core SO257-18548 is located ~7 nm west of IODP Site U1482 at the western edge of an elevated plateau that forms the northeastern part of the Rowley Terrace between the Scott Plateau and Exmouth Plateau. Core SO257-18548 was retrieved during a site survey in the vicinity of IODP Site U1482. The main objective of coring at this location was to recover the late Pleistocene to Recent sedimentary record, which is missing at Site U1482, as a local sediment gravity flow eroded sediments younger than MIS 9. Recovered sediments consist of homogenous mottled olive greenish gray to dark gray clay-rich calcareous ooze (Kuhnt et al., 2018; Rosenthal et al., 2018; Supplementary Figure S1).

Gravity Core SO257-18571 (22° 6,666'S, 113° 29,688'N, 1052 m water depth, 20.1 m core length) was retrieved offshore the North West Cape Peninsula south of the Exmouth Plateau (Figure 2). The core is located within the “dust-cyclone” climate belt at the northern end of the arid climatic zone in Western Australia and is only marginally affected by the austral summer monsoon rain belt. This area receives mainly water and sediment from the Ashburton, Fortescue, Gascoyne and De Grey Rivers, which sporadically have high discharges following torrential rainfall after the landfall of tropical cyclones (Figure

2C). Core SO257-18571 is located at the western edge of an E-W orientated ridge at a position, where 8 khz seismic reflectors indicated locally higher sedimentation rates. Recovered sediments consist of clay-rich nannoplankton ooze with distinct intercalations of dark reddish brown, clay-rich intervals and light olive gray calcareous ooze (Kuhnt et al., 2018; Supplementary Figures S2 and S3).

3.2. Sampling and processing

The working halves of Cores SO257-18548 and -18571 were initially sampled at 10 cm intervals (1 cm-thick half slices of 11 cm diameter cores). Additional samples were taken over Termination I (6 samples from Core SO257-18548 between 94.5 and 204.5 cm depth) and Termination II (10 samples from Core SO257-18548 between 456.5 and 576.5 cm depth) to refine the age model. Four holes were cored at Site U1482 during IODP Expedition 363 (Rosenthal et al., 2017, 2018). The working halves from the composite sediment succession (shipboard splice) between 24.76 and 30.22 meters composite depth (mcd) were sampled at 20 cm intervals (2 cm-thick half slices of ~7 cm diameter cores). The sediment succession from Core SO257-18548 and nearby Site U1482 were combined based on correlation of the high-resolution XRF scanner elemental records (Supplementary Figures S4 and S5). The tie point, corresponding to an age of ~324 ka, is located at 10.84 m in Core SO257-18548 and at 24.97 mcd in Site U1482. All samples were oven dried at 40°C and weighed prior to washing over a 63 µm sieve. Residues were oven dried at 40°C on filter paper, then weighed and sieved into the fractions >315, 315-250, 250-150 and 150-63 µm.

3.3. Stable isotope analysis

Stable oxygen isotopes of the epibenthic foraminifer *Cibicidoides wuellerstofi* were measured in 132 samples from Core SO257-18548, 28 samples from Site U1482 and 150 samples from Core SO257-18571. In each sample, 3-6 well-preserved specimens of *C. wuellerstofi* were picked from the fraction >315 µm and/or 315-250 µm. Selected well-preserved specimens were crushed into large fragments, agitated with ethanol for 2-3 s in an ultrasonic bath, decanted and dried at 40 °C prior to analysis with a Thermo Finnigan MAT 253 mass spectrometer at the Leibniz Laboratory for Radiometric Dating and Isotope Research, Kiel University, Kiel. The mass spectrometer is coupled to a *Kiel-Carbo IV* device for automated CO_2 preparation from carbonate samples. Sample reaction was induced by individual acid addition (99 % H_3PO_4 at 75 °C) under vacuum. The evolved carbon dioxide was analysed eight times for each individual sample. As documented by the performance of international [NBS19: +1.95 ‰ VPDB (^{13}C), -2.20 ‰ VPDB (^{18}O); IAEA-603: +2.46 ‰ VPDB (^{13}C), -2.37 ‰ VPDB (^{18}O)] and laboratory-internal carbonate standards [Hela1: +0.91 ‰ VPDB (^{13}C), +2.48 ‰ VPDB (^{18}O); HB1: -12.10 ‰ VPDB (^{13}C), -18.10 ‰ VPDB (^{18}O); SHK: +1.74 ‰ VPDB (^{13}C), -4.85 ‰ VPDB (^{18}O)] , analytical precision of stable isotope analysis is better than ±0.08 ‰ for δ^{18}O and better than ±0.05 ‰ for δ^{13}C. Values are calibrated relative to Vienna Pee Dee Belemnite.

3.4. Age models

Between 0 and ~21 ka, the age models of Cores SO257-18548 and -18571 are based on ^{14}C dates obtained from the surface-dwelling planktonic foraminifer *Globigerinoides ruber* (white). Between 600 and 800 specimens of the planktic foraminifer *G. ruber* >250 µm were picked for AMS dating in order to reach a sample weight of 12 mg. In both cores, we selected samples at depths close to the transition between the Bølling-Allerød and the Younger Dryas and close to the center of the LGM. Samples were measured at the Leibniz Laboratory for Radiometric Dating and Isotope Research, Kiel University, Kiel. Conventional radiocarbon ages were converted into calendar ages using Calib 7.1 (Stuiver et al. 2019). We applied a marine reservoir age of 510 years for the sample at a depth of 70 cm in Core 18548 (>13 ka), 200 years for the sample at a depth of 140 cm in Core 18571 (>10 ka) and 1600 years for the samples at a depth of 100 cm in Core 18548 and at a depth of 190 cm in Core 18571 (<20 ka), following corrections determined at the nearby Core MD01-2378 (Sarnthein et al., 2011).

For the interval older than 21 ka, we derived age models for Cores SO257-18548 and -18571 and for Site U1482 (between 24.76 and 30.22 mcd) by correlating the benthic foraminiferal $\delta^{18}O$ records to the reference benthic isotope stack LR04 (Lisiecki and Raymo, 2005), using linear interpolation between tie points (Linage) in AnalySeries 2.08 (Paillard et al., 1996).

3.5. XRF scanner derived elemental composition

Bulk-chemical composition of the sediment cores was determined using a 2nd generation Avaatech XRF core scanner at the Institute of Geosciences, Kiel University. Before measurement, the sediment surface was smoothed and covered with a 4.0 µm thick Prolene® Thin-Film foil to minimize surface irregularities and to avoid direct contact between the sediment and the detector. Measurements were carried out on the archive halves at 1 cm intervals over a 1.2 cm^2 area with a down core slit size of 10 mm, using generator settings of 10, 30 and 50 kV tube voltages. We performed measurements for 15 seconds with 200 µA without filter for the 10 kV runs and for 10 seconds with 1000 µA using a Pb and Cu-filter for the 30 and 50 kV runs, respectively. The spectra were transferred into elemental area counts using the software bAxil Batch by Brightspec NV and are reported as area counts per second. Results are reported in logarithms of elemental ratios, which provide the most easily interpretable signals of relative changes in chemical composition downcore and minimize the risk of measurement artefacts from variable signal intensities and matrix effects (Weltje and Tjallingii, 2008).

We used the sum of the spectral area counts of the elements aluminium (Al), silicon (Si), potassium (K), iron (Fe), titanium (Ti) as proxies for the terrigenous derived sediment component (abbreviated as "Terr") mainly originating from riverine transport from the Australian continent. We normalized these elements against calcium (Ca), derived from the biogenic carbonate of marine plankton. An alternative normalization was performed against barium (Ba), which is related to particulate organic matter and/or the precipitation of barite by marine bacteria and is, thus, independent of carbonate production and dissolution. The Log(Terr/Ba) curve exhibit similar trends in all cores as Log(Terr/Ca),

suggesting that the variability of these records is mainly driven by increasing or decreasing terrigenous flux (Supplementary Figure S6). Core scanner measurements of the split core sediment surface commonly underestimate concentrations of the light elements Al and Si, due to the influence of pore water in unconsolidated sediment (Tjallingii et al., 2007). However, replicate XRF scanner measurements of compressed dry powder from the same core interval show that pore water bias affects only the uppermost ~100 cm of our cores. The Log(Al/Ca) and Log(Si/Ca) curves in this interval become noisier in both cores, but do not substantially differ from curves of the heavier elements (Log(K/Ca), Log(Ti/Ca), and Log(Fe/Ca)) over the last glacial termination and Holocene (Supplementary Figure S7A and B).

Differences in the abundance of zirconium (Zr) and light elements (Al, K or rubidium (Rb)) reflect the grain size and transport pathway of terrigenous particles, since K, Al and Rb are preferentially incorporated in river-transported fine-grained clay, whereas larger and/or heavier wind-blown grains from the Australian desert have relatively high Zr values. Zirconium is the main component of the heavy mineral zircon, which is subject to sorting and preferential settling close to river mouths and on the continental shelf, and thus mainly characterizes wind transported dust at distal locations. In particular, Zr/Rb in sediment has been shown to reflect the initial grain size distribution (coarser sediment Zr-enriched, finer sediments clay mineral bound Rb-enriched) of wind-blown sediments, due to the immobility of the two elements during post depositional processes (Liu, 2002).

3.6. Calibration of XRF scanner data by melt XRF analysis of discrete samples

To calibrate the XRF scanner data, 11 homogenized and discrete samples of the terrigenous sediment component from Core SO257-18571 and 9 samples from Core SO257-18548 were analysed using quantitative XRF analysis of fused beats. For discrete sample measurements, all samples were decarbonatized by adding 10 % HCl until the reaction stopped. The suspension was neutralized after centrifugation for 10 min at 3000 revolutions/min, decanted and refilled with deionized water. This neutralization was repeated six times. The neutralized suspension was wet sieved over a 63 µm sieve and the fine fraction (<63 µm) collected and filled into beakers. After 5 weeks, the supernatant was carefully pumped out. After drying at 50°C, aliquots of each sample were used to produce fused beads and pressed pellets (Garbe-Schönberg and Müller, 2014). Fused beats were produced by mixing the sample material with lithium-tetraborate and heated to ~1050 °C. Major and trace elements were determined on the fused lithium-tetraborate glass disks with a X-ray fluorescence spectrometer (XRF - Panalytical MagixPro) at Hamburg University using the software of Vogel and Kuipers (1987). Accuracy was controlled by analyses of several international standards. The precision of the instrument is 1-2 % for major elements and 5–20 % for trace elements depending on the concentration. Loss on ignition (LOI) was determined gravimetrically after heating the samples to 1050 °C for 3 hours (Lechler and Desilets, 1987). Pressed pellets were produced by grinding down the dried material first with a mortar and afterwards with a Pulverisette 7 premium line from Fritsch, pressed into pellets and measured with the second generation Avaatech XRF core scanner at the Institute of Geosciences, Kiel University. Analytical results of

quantitative fused beats XRF and corresponding XRF scanner area counts for Core SO257-18548 are provided in Supplementary Table S1A and B and for Core SO257-18571 in Supplementary Table S2A and B. Linear regression plots are shown in Supplementary Figure S8.

3.7. Elemental signatures of Western Australian river sediments

To determine the provenance of the terrigenous component of marine sediments, samples from Core SO257-18548 (core-top samples) and Core SO257-18571 (core depth 113.5 cm) were compared with fine-grained (<63 μm) sediments from the main rivers in northwestern Australia. The chemical composition of marine and river sediments was analyzed by melt XRF analysis of discrete samples. Aliquots of the same samples were additionally analyzed in discrete pellets with the XRF scanner at Kiel University. After decarbonatization, the samples were pulverized in an agate mortar and pressed into pellets with a Pulverisette 7 premium line from Fritsch, then analyzed with the XRF core scanner at Kiel University.

4. Results

4.1. Chronology and sedimentation rates

Between 0 and ~21 ka, the age models of Cores SO257-18548 and -18571 are based on ^{14}C AMS dates (Table 1). To derive age models prior to 21 ka in Cores SO257-18548 and -18571 and at Site U1482, we selected consistent tie points between the benthic foraminiferal δ^{18}O curves and the reference benthic isotope stack LR04 (Lisiecki and Raymo, 2005) (Table 2, Figures 3-4). For the interval from 24.76 to 30.22 mcd at Site U1482, shipboard biostratigraphic datums provided additional age constraints between 0.29 to 0.44 Ma (Rosenthal et al., 2018) (Figure 3).

Sedimentation rates (SR) in Core SO257-18571 exhibit a distinct glacial-interglacial variability (Figure 4). Mean SR range between 8.6 cm/kyr during MIS 5e and 11.5 cm/kyr during the Holocene, whereas mean SR are substantially lower during glacial periods, varying between 3.7 cm/kyr during MIS 6 and 4.5 cm/kyr during the LGM. Sedimentation rates during MIS 3, 4 and 5a-d also remain low, as during the LGM and MIS 6. By contrast, sedimentation rates for Core SO257-18548 and at Site U1482 show more consistent trends of 2.5 to 5.5 cm/kyr without major glacial and interglacial differences (Figure 3).

We additionally tested the robustness of the age models by correlating our oxygen isotope records to the Antarctic δD derived temperature record (Bazin et al., 2013). Within the range of error in our intermediate resolution (~2-4 kyr) isotope records, the onset of glacial terminations occurs simultaneously, whereas the end of glacial terminations (temperature maximum) is 2 to 5 kyr later in the marine record (Supplementary Figure S9).

4.2. Composition and provenance of terrigenous sediment discharge

Comparison of the terrigenous elemental composition of Core SO257-18548 with that of the riverine sediment discharge from the Kimberley coast, which is the closest sediment source on the

Australian continent shows a high degree of affinity (Figure 2, Table 3). In particular, the terrigenous component of Core SO257-18548 is very close to that of the fine-grained clay-fraction dominating the King Sound sediment near Derby, where the Fitzroy River enters into the shelf sea. The coarser grained, silt-dominated sediment, sampled upstream of the Fitzroy River exhibits higher Si percentages, which is mainly due to the higher quartz content of the silt fraction. The elevated K content is typical for this area, which agrees with clay mineral analyses showing higher percentages of the K-rich clay mineral illite (Gingele and DeDeckker, 2004). In the vicinity of the Northwest Cape Peninsula, the sediment loads of the Ashburton, Fortescue and Gascoyne Rivers exhibit similar elemental compositions with higher Fe concentrations, which are closely reflected in the composition of the Holocene terrigenous sediment fraction in Core SO257-18571, located offshore from these rivers (Figure 2, Table 3).

4.3. Variations in riverine terrigenous sediment input

Log (Terr/Ca) is used to estimate the contribution of terrigenous sediment discharge normalized against the marine biogenic carbonate flux, which is considered to be relatively constant offshore northwestern Australia (Kuhnt et al., 2015). In Cores SO257-18571 and -18548 and at Site U1482, Log (Terr/Ca) shows glacial-interglacial variability that is generally coherent with the $\delta^{18}O$ records (Supplementary Figure S10A). In Core SO257-18548, glacial-interglacial (~100 kyr) coherence is >0.8 with an out-of-phase relationship (highest Log(Terr/Ca) coincide with lowest $\delta^{18}O$), while coherence at the precessional band (23 kyr) is highest (0.83). However, there is a distinct mismatch between $\delta^{18}O$ and terrigenous runoff during MIS 5a and 5c, when terrigenous runoff remains comparable to glacial levels in Cores SO257-18548 and -18571. In Core SO257-18571, coherence is highest (~0.85) at the glacial-interglacial scale, whereas it is lower (~0.76) at the precessional band (Supplementary Figure S10B).

During glacial stages, mean Log(Terr/Ca) is distinctly lower in Core SO257-18571 than in Core SO257-18548, with a minimum value of -1.5 during MIS 5d to MIS 2 and higher values of -1.2 to -1.3 during MIS 8 and MIS 6, respectively. In Core SO257-18548, mean Log(Terr/Ca) is -1.1 for MIS 5d and MIS 2 and -0.9 for MIS 8 and MIS 6. Maximum values are reached in both cores as distinct sharp peaks at the end of glacial terminations or at the beginning of interglacials: at ~10 ka (end of Termination I/early Holocene), ~130 ka (end of Termination II/early MIS 5e), ~200, ~220 and ~240 ka (end of Termination III/ early MIS7 and precessional insolation maxima within MIS 7) and at ~280, ~305 and ~330 ka (end of Termination IV/early MIS 9 and precessional insolation maxima within MIS 9 and MIS 8). Maxima are comparable (between -0.2 and -0.5) in both cores, although minima are distinctly lower in Core SO257-18571, suggesting a higher amplitude change of sediment discharge from the semi-arid zone in northwestern Australia than from catchments within the monsoonal rainbelt. In addition, the deglacial onset of enhanced discharge from the semi-arid zone was more rapid, in particular during Termination II, when Log(Terr/Ca) in Core SO257-18548 already exhibits an increasing trend in the late MIS 6, whereas Core SO257-18571 Log(Terr/Ca) shows an abrupt change point at the onset of the glacial termination. The

runoff pattern across MIS 11 differs markedly from the later interglacial trends: the Log(Terr/Ca) curve is almost symmetrical without a distinct peak in the early part of the interglacial.

Accumulation rates of the terrigenous component in Core SO257-18571 are lower than ~1 g/(cm^{2}kyr^1) during glacial MIS 2-4, 6 and 8 and reach maxima of >4 g/(cm^{2}kyr^1) during interglacial MIS 9, 7, 5e and 1 (Supplementary Figure S11). The increases in accumulation rates occur abruptly close to the end of glacial terminations in parallel to increases in carbonate accumulation associated with increasing biogenic carbonate production (Supplementary Figures S11 and S13). The deglacial increase in terrigenous accumulation rates in Core SO257-18548 is less dramatic and restricted to MIS 7 and MIS 1, while the accumulation rates of both the carbonate and terrigenous components remain low during MIS 5e (Supplementary Figures S11 and S12). Carbonate accumulation rates are below ~1 g/(cm^{2}kyr^1) during MIS 5e, which is lower than during the preceding glacial stage. During MIS 5d to MIS 5a, carbonate accumulation rates increase continuously, then fluctuate at ~2 g/(cm^{2}kyr^1) during MIS 4 to 2, which is ~0.5 g/(cm^{2}kyr^1) lower than average Holocene values. In contrast, changes in sedimentation rates between glacial and interglacial stages at Site SO257-18548 are relatively low or even absent in the case of MIS 5, although the sediment composition changes significantly from carbonate dominated during glacials to terrigenous clay dominated during interglacials.

4.4. Variations in dust input

Log (Zr/Rb) in Core SO257-18571 exhibits a distinct glacial/interglacial cyclicity, in contrast to the record from Core SO257-18548 and Site U1482, which shows relatively low values with only subtle shifts between glacial and interglacial periods. This distinct cyclicity in Core SO257-18571 parallels the oxygen isotope trend and is in antiphase to that of Log (Terr/Ca). The abrupt decreases in dust input and increases in riverine terrigenous input of clay minerals occur almost simultaneously during Terminations I, II and III. During interglacial periods, Log (Zr/Rb) remains low, ranging between 0.28 and 0.5 (20 point smoothed data), whereas mean values are high (0.6 to 1.0) during glacial stages. Parallel to the marked decrease in Log (Terr/Ca) at the end of MIS 5e, Log (Zr/Rb) displays the largest increase within the record and exhibits a distinct maximum during MIS 5d. Between this maximum and the next pronounced peak during the LGM, three smaller maxima with an amplitude ≤0.2 occur. These peaks approximately coincide with the cold MIS 5b and MIS 4 intervals and the central part of MIS 3 (Figure 5). Between the LGM and the Holocene, Log (Zr/Rb) decreases markedly once again. This decline is not continuous, but is interrupted by small plateaus at ~ 25 to 23 ka, ~ 21 to 17.5 ka, and ~ 14 to 10 ka. During the Holocene, Log (Zr/Rb) ranges between 0.27 and 0.43 with a standard deviation of 0.03.

5. Discussion

5.1 Reconstruction of monsoonal discharge

Terrigenous flux reconstructions are based on XRF scanner derived concentrations of Al, Si, K, Fe and Ti. These elements are commonly used to estimate the proportion of terrigenous (lithogenic) content in marine sediments, however, there are various caveats associated with each element. The concentration of Al is preferentially used to estimate the total lithogenic content of sediments because its concentration is very consistent in the continental lithosphere (Turekian and Wedepohl, 1961; Wedepohl, 1971; Taylor and McLennan, 1985). Silicon is present in all aluminosilicates and also occurs as quartz (SiO_2), which is the main component in the silt fraction of sediments and sedimentary rocks (Calvert and Pedersen, 2007). Core scanner measurements of the split-core sediment surface commonly underestimate concentrations of the light elements Al and Si, due to the influence of pore water in unconsolidated sediment (Tjallingii et al., 2007). However, replicate XRF scanner measurements of compressed dry powder from the same core interval show that pore water bias affects only the uppermost ~100 cm of our cores and does not substantially affect the shape of the Log(Terr/Ca) curve over the last glacial Termination and Holocene (Supplementary Figure S6).

Potassium predominantly occurs as a component of the clay mineral illite in fine-grained riverine runoff. Its concentration is reliably estimated by the XRF scanning technique (Tjallingii et al., 2007) and it has been previously used to monitor monsoonal riverine runoff across the last glacial termination (Kuhnt et al., 2015). Iron and Ti were used to evaluate the changing input of fine-grained terrigenous siliciclastic sediment from adjacent continental margin offshore Venezuela and Java (Jansen et al., 1998; Mohtadi et al., 2011; Haug et al., 2001), which was driven by variations in rainfall and runoff from the watersheds of local rivers. However, Ti usually exhibits fairly low counts, when analysed with the XRF scanner, and the Fe content may be partly biased by the formation of authigenic iron/manganese crusts or pyrite (Calvert and Pederson 2007; Poulton and Raiswell, 2002).

Using the sum of terrigenous elements instead of individual elements reduces the noise in XRF scanner data, since this produces higher counts and reduces the effects of possible biases in single element counts. Here, we used the logarithmic ratio of the sum of the terrigenous elements Al, Si, K, Fe, and Ti to Ca (Log(Terr/Ca)). This approach is commonly used in carbonate-rich pelagic environments, where carbonate dissolution plays no major role (Kuhnt et al., 2015). The carbonate concentrations vary between 54 and 80.5 % in Core SO257-18548 and between 50 and 86 % in Core SO257-18571. We assume that the variability in Log(Terr/Ca) in these two cores is mainly driven by changes in terrigenous input. Calcium is relatively rare in terrigenous sediments and in marine deep-water environments mainly derived from biogenic carbonate. To further test this hypothesis, we normalized against Ba (Supplementary Figure S6), which is related to particulate organic matter flux and/or the precipitation of barite by marine bacteria (Gonzalez-Munoz et al, 2012; Griffith et al, 2012) and, thus, has no direct relation to carbonate flux. In previous records from the northwestern Australian margin, $CaCO_3$ and organic productivity indicators such as total organic carbon (TOC) and chlorins did not show any positive correlation (Holbourn et al., 2005). Thus, we conclude that the consistent behaviour of terrigenous elements normalized against Ca or Ba

indicates that fluctuations in the Ca-normalized terrigenous elemental curves are caused by fluctuations in terrigenous input rather than changing marine carbonate production/dissolution.

5.2 Monsoonal response to changes in atmospheric greenhouse gas concentrations and high-latitude temperature fluctuations

Model predictions of changes in the latitudinal extent of the ITCZ's seasonal swing and the development of an interhemispheric seesaw during the last glacial cycle are contradictory and not fully supported by climate proxy data, which are still scarce for the Southern Hemisphere (Denton et al., 2010; Shakun et al., 2012; De Deckker et al., 2012; Kuhnt et al., 2015). In particular, increasing greenhouse gas concentrations during HS 1 (Lüthi et al., 2008; Shakun et al., 2012) should have resulted in tropical expansion (Seidel et al., 2008) at the end of the LGM. Expansion and contraction of the monsoonal rain belt triggered by greenhouse gas concentrations is supported by a comparison of high-resolution Northern and Southern Hemisphere speleothem records over the last three millennia, which indicates coeval intensification/poleward shift and weakening/equatorward shift of monsoonal rain belts on suborbital timescales in both hemispheres (Denniston et al., 2016). However, substantial regional cooling associated with widespread drying in the subtropics and tropics in the Northern Hemisphere during HS 1 and preceding Heinrich stadials was attributed to a southward shift of the ITCZ and associated monsoonal rain belt (Claussen et al., 2003; Chiang and Bitz, 2005; Chiang et al., 2003, 2008; Broccoli et al., 2006; Muller et al., 2008, 2012; Bayon et al., 2017; Strikis et al., 2018; Lauterbach et al., 2020). By contrast, a recent compilation of model ensembles for different forcings demonstrated the importance of additional forcings on the variability of the ITCZ, including disturbance of the global ocean circulation by North Atlantic hosing and LGM boundary conditions (Atwood et al., 2020). While insolation differences between hemispheres and atmospheric pCO_2 are important, they may not alone force a mean shift of the tropical rainbelt. Moreover, precipitation proxy data compilations demonstrated that the height of HS 1 coincided with a latitudinally widespread drought, which also affected the Southern Hemisphere (Stager et al., 2011). According to these authors, the widespread geographic range of aridification during HS 1 suggests a severe weakening of the tropical rainfall systems probably as a response to global sea surface cooling.

Our high-resolution runoff records from Core SO257-18548 and Site U1482, and from Core SO257-18571 also exhibit no distinct increase in riverine discharge in the early part of Termination I, suggesting that northwestern Australia remained largely arid during HS 1. A massive and rapid increase in riverine discharge started only at ~13 ka at these sites following the Antarctic Cold Reversal (~15-13 ka). This is consistent with records within the core area of the Australian monsoonal rain belt further to the northeast, where terrigenous runoff also did not significantly increase prior to 13 ka (Kuhnt et al., 2015). These generally dry conditions were only locally interspersed by transient rainfall episodes during HS 1, HS 2, and HS 4, as indicated by composite stalagmite $\delta^{13}C$ records from caves in the Kimberleys in northwestern Australia (Denniston et al., 2017). On orbital timescales, it is remarkable that the ITCZ appears to have consistently remained in a more northerly position during MIS 5b and 5d and associated

stadials and that northwestern Australia remained consistently dry and dusty. By contrast, eastern Australia experienced increased precipitation linked to southward expansion of the ITCZ (Bayon et al., 2017). Recent modelling studies underline the role of longitudinally variable responses of the ITCZ to different climate forcings (Atwood et al., 2020) which could explain different responses to Northern Hemisphere cooling in eastern (Bayon et al., 2017; Muller et al., 2008) and western Australia.

Although our records do not resolve short-term local precipitation changes, they may provide a better estimate of time- and regional-averaged long-term precipitation and runoff trends on millennial timescales. The dampened response to changes in the interhemispheric temperature gradient in these "smooth" records supports the hypothesis of global subtropical megadroughts during intervals of globally cool climate and low atmospheric pCO_2. Major wet periods in northwestern Australia are restricted to warmer-than-present climate intervals in the early Holocene (~10 ka), early MIS 5e (~130 ka), MIS 7 (~200, ~220 and ~240 ka), and MIS 9 (~280, ~305 and ~330 ka), when monsoonal rainfall also increased in many Northern Hemisphere monsoonal regions (Liu et al., 2014; Cheng et al., 2016; Kathayat et al., 2016). In particular, the intense monsoonal peaks centered at ~10, ~130, ~240 and ~330 ka, which follow Southern Hemisphere high-latitude temperature maxima at the end of glacial terminations (Figure 6), suggest an enhanced regional response of the Australian Monsoon, driven through internal feedbacks. The general coherence between the intensity of the Australian Monsoon and global pCO_2 and climate trends is also reflected in the high coherence and consistent antiphase behavior of benthic $\delta^{18}O$ and monsoonal discharge in our records (Supplementary Figure S10). Model experiments with warm Pliocene boundary conditions indicated that an intensification of subtropical precipitation in both hemispheres may have been driven by reduced meridional sea-surface temperature gradients in a warmer world (Burls and Fedorov, 2017) and was decoupled from shifts of the ITCZ on millennial timescales (Sniderman et al., 2019).

5.3 Temporal changes in the extent of the northwestern Australian arid zone

Today, estimates of terrigenous dust accumulation off northwestern Australia range between 1 and 5 g/(m^2yr^1) (Jickells et al., 2005), which represents ~2-5 % of the total sediment mass accumulation or >10 % of the terrigenous component at marine sites within the dust belt with typical deglacial sedimentation rates of ~5 cm/kyr^1 (Figure 1A)(Kuhnt et al., 2018). The proportion of dust-blown sediment considerably decreases towards the northeast, where sedimentation rates increase and dust accumulation decreases, implying that a substantial proportion of the Zr, Ti and Fe content is of aeolian origin only at the southerly location of Core SO257-18571. The aeolian terrigenous material that reaches distal marine locations is usually deposited during extreme dust outbreaks (Rea, 1994). The occurrence of discrete Zr-, Ti- and Fe-enriched layers in the glacial intervals of Core SO257-18571 may, thus, represent a record of major dust storms (Rea, 1994; Hanebuth and Henrich, 2009).

Riverine transported fine-grained terrigenous discharge and aeolian dust input in Core SO257-18571 exhibit a clear antiphase relationship with no recognizable phase lags, suggesting coeval and abrupt changes towards wetter climate and increased fluvial discharge during glacial terminations and rapid re-

aridification at the end of the unusually warm isotope stages MIS 9, 7 and 5e. Increased dust transport to the eastern Indian Ocean implies a reduced vegetation cover during periods of increased seasonal aridity in the source area, following changes in preferential wind direction and/or strengthening of winds. The rapid intensification of monsoonal rainfall and re-aridification at the onset and end of the warmest intervals with highest atmospheric greenhouse gas levels suggest that these rapid transitions were defined by transgressing boundary condition thresholds. However, there are striking differences in the sedimentation processes and the climate of the catchment area at the locations of Core SO257-18548 and Site U1482 within the monsoonal belt and of the more southwestern Core SO257-18571 within the dust-cyclone belt. Precipitation in the arid zone almost exclusively occurs during the landfall of major tropical cyclones, which form in the tropical Indian Ocean during the monsoonal season, when SST thresholds of 26-27°C are reached (Tory and Dare, 2015). Increased cyclone activity during monsoon intensification is also reflected by massive increases in sedimentation rates during the warm stages MIS 1, MIS 5e and the warm parts of MIS 7 and MIS 9 in Core SO257-18571 (Figure 4), whereas sedimentation rates in Core SO257-18548, which is dominated by seasonal monsoonal discharge, remain more consistent (Figure 3). Southern Hemisphere subtropical sea surface temperatures may have played a major role in setting these boundary conditions. However, boundary conditions remained below the threshold necessary for the formation of tropical cyclones during the slightly cooler interglacial MIS 5a and MIS 5c, which remained dry and dusty within the dust-cyclone belt (Figure 5).

5.4 Monsoon forcing mechanisms

The intensity, seasonality and latitudinal extent of monsoonal rainfall during the summer season depend on the seasonal displacement of the ITCZ, which is influenced by insolation differences between the Northern and Southern Hemisphere (Broccoli et al., 2006) and is also highly sensitive to greenhouse gas forcing (Cai et al., 2012). However, the response of the ITCZ to interhemispheric insolation and temperature differences appears regionally variable and dependent on additional local forcings (Atwood at al., 2020). Sedimentary successions at the more northeasterly situated Site U1483 and Core MD01-2378 in the Timor Sea display a similar monsoonal runoff pattern as Core SO257-18548 and Site U1482 (Zhang et al., 2020). The runoff record at these locations exhibits in-phase variability with Northern Hemisphere monsoonal precipitation records on the precession band, which was interpreted as an expansion (contraction) of the latitudinal extent of the ITCZ during Northern Hemisphere insolation maxima (minima) (Zhang et al. 2020).

Our comparison of two sedimentary succession providing a transect across the southernmost limit of the Australian Monsoon shows that regional factors additionally play a crucial role in controlling the seasonal position of the ITCZ and intensity of monsoonal rainfall over northwestern Australia. In particular, the seasonal and interannual heat and air pressure variability over the more elevated Pilbara area acts as a main driver of monsoonal hydroclimate. In austral winter and spring, subtropical high-pressure systems are positioned over the central part of the Australian continent forcing dry easterly or

southeasterly Trade Winds over the Pilbara region, thus maintaining intensely arid conditions (Charles et al., 2015; Sudmeyer, 2016). The seasonal southward movement of subtropical high-pressure systems in September results in the dominance of tropical heat lows over the Pilbara region during the extremely hot and dry spring and the summer wet season. The position of this heat low is related to the location of the Pilbara region between the relatively cooler marine area to the north and latitudinally decreasing solar insolation to the south. In recent decades, an expansion of the Southern Hemisphere Hadley Cell in association with global warming caused a northward shift of frontal systems at the northern end of the Hadley Cell during austral winter and intensification of winter aridity in the Pilbara region (Lu et al., 2007; Risbey et al., 2009; Frederiksen et al., 2013).

The most intense phase of the heat low, which occurs in spring and early summer (September-November), precedes the monsoon season and is not associated with local rainfall (Charles et al., 2009). However, the intensity and position of the heat low have significant repercussions in "pulling" the monsoonal rain belt southwards, resulting in a coupled relationship between the strength of the monsoonal circulation and associated heavy rainfall with the intensity of the heat low (Suppiah, 1992). Important controlling factors on the variability in the intensity and position of the heat low on multidecadal, millennial and orbital timescales include (1) the precessional variability of spring (September-October) Southern Hemisphere orbital insolation, (2) the insolation gradient between tropical (~10°S) and subtropical (~30°S) insolation, which prevents the heat low from moving southwards into areas of lower insolation when the gradient is steep and, (3) the concentration of atmospheric greenhouse gases, which contributes to the intensity of the heat low. During the last 450 kyr, maxima in these three factors occurred at ~10, ~130, ~200, ~220, ~240, ~280, ~305 and ~330 ka, when terrigenous flux from monsoonal runoff strongly increased or was at a maximum, mostly close to the end of glacial terminations (Figures 6-7, Supplementary Figure S14).

During MIS 12 to 10, insolation forcing over the Pilbara region was minimal and the insolation gradient between 10 and 30°S remained elevated, which resulted in a more gradual monsoonal onset with muted response to precessional forcing. This weaker and more gradual monsoon intensification at the end of glacial Termination V (MIS 11) may have been additionally affected by pronounced vegetation changes leading to lower austral spring albedo of the Pilbara mountains. Palynological data indicate a major change in northwestern Australian subtropical vegetation patterns and hydroclimate associated with the onset of intense aridification at ~350 ka during MIS 10 (Kershaw et al., 2003; Kawamura et al., 2006). This major, long-term change in Australian subtropical hydroclimate was associated with the Mid-Brunhes Climate Transition (Jansen et al., 1986; Barth et al., 2018), which occurred during an interval of low precessional insolation forcing between 430 and 350 ka and was followed by an increase in the amplitude of the Earth's 100 kyr glacial-interglacial climate cycles.

Atmospheric methane concentration records in ice cores exhibit extreme spikes associated with glacial terminations, which closely match the main atmospheric CO_2 peaks (Figure 6) (Loulergue et al., 2008). The origin of these short-lived millennial scale methane maxima in the atmosphere has been

intensely discussed with high-latitude permafrost and peatlands and low-latitude monsoonal wetlands being the prime candidates as the main sources for the rapid atmospheric methane increase (Chappellaz et al., 1990; Guo et al., 2011; Thirumalai et al., 2020) that may have contributed to the interhemispheric synchronization of glacial terminations. Low-latitude hydroclimate and vegetation changes, thus, may have contributed to intensified greenhouse gas release in subtropical regions and development of global methane and pCO_2 maxima during glacial terminations (Rhodes et al., 2015; Bock et al., 2017).

6. Conclusions

XRF scanner derived increases in terrigenous discharge indicate rapid intensification of the Australian Monsoon at the end of glacial terminations with short-lived peaks in the early Holocene (~10 ka), MIS 5e (~130 ka), MIS 7 (~200, ~220 and ~240 ka), and MIS 9 (~280, ~305 and ~330 ka). The correlation of monsoonal precipitation and runoff proxies and Antarctic temperature, CO_2 and CH_4 concentrations during the last five glacial terminations suggests that the intensification of heat low pressure cells over northwestern Australia at the end of glacial terminations was mainly driven by rapidly increasing atmospheric greenhouse gas concentrations in conjunction with a low insolation gradient between Southern Hemisphere tropics and subtropics and rising and/or high Southern Hemisphere spring-early summer insolation. The formation of intense heat low pressure cells in the Pilbara region of northwestern Australia in late September may have played a crucial role in driving the ITCZ southwards and triggering intensified monsoonal rainfall on orbital timescales, when Southern Hemisphere insolation was at a maximum. Changes in riverine terrigenous sediment supply at the onset of MIS 11 were more gradual and do not indicate an abrupt change from arid to monsoonal wet conditions, suggesting that an extended period of low variability in precessional spring insolation and expanded vegetation cover over northwestern Australia weakened the heat low pressure cell over the Pilbara mountains. Southward swings of the ITCZ amplified and deglacial monsoonal onsets intensified with aridification of northwestern Australia ~350 kyr ago.

Acknowledgements

This research used data and samples provided by the International Ocean Discovery Program (IODP). We are grateful to the Sonne 257 and IODP Expedition 363 shipboard scientific parties for all their efforts. Renjie Pei gratefully acknowledges financial support from the State Scholarship Fund of China Scholarship Council. We thank Matthias Hüls for AMS ^{14}C analyses at the Leibniz Laboratory for Radiometric Dating and Isotope Research, Kiel and Stefan Jung for fused beat XRF measurements at the Institute of Mineralogy and Petrography in Hamburg. We are grateful for constructive comments from two anonymous reviewers, which helped us to improve the manuscript. This study was funded by the German Federal Ministry of Education and Research (Grant SO-257, WACHEIO, 03G0257A).

Conflict of interest

The authors declare that they have no conflict of interest.

Supplementary data

Supplementary materials

References

Atwood, A.R., Donohoe, A., Battisti, D.S., Liu, X., Pausata, F.S.R., 2020. Robust Longitudinally Variable Responses of the ITCZ to a Myriad of Climate Forcings. Geophys. Res. Lett. 47. doi:10.1029/2020GL088833

Barth, A.M., Clark, P.U., Bill, N.S., He, F. and Pisias, N.G., 2018. Climate evolution across the Mid-Brunhes Transition. *Climate of the Past*, *14*(12). doi:10.5194/cp-14-2071-2018

Bayon, G., De Deckker, P., Magee, J.W., Germain, Y., Bermell, S., Tachikawa, K., Norman, M.D., 2017. Extensive wet episodes in Late Glacial Australia resulting from high-latitude forcings. Sci. Rep. 7, 1–7. doi:10.1038/srep44054

Bazin, L., Landais, A., Lemieux-Dudon, B., Kele, H.T.M., Veres, D., Parrenin, F., Martinerie, P., Ritz, C., Capron, E., Lipenkov, V. and Loutre, M.F., 2013. An optimized multi-proxy, multi-site Antarctic ice and gas orbital chronology (AICC2012): 120-800 ka. *Climate of the Past*, European Geosciences Union (EGU), 2013, 9 (4), pp. 1715-1731. doi:10.5194/cp-9-1715-2013

Bock, M., Schmitt, J., Beck, J., Seth, B., Chappellaz, J., and Fischer, H., 2017. Glacial/interglacial wetland, biomass burning, and geologic methane emissions constrained by dual stable isotopic CH_4 ice core records. PNAS, E5778-E5786. www.pnas.org/cgi/doi/10.1073/pnas.1613883114

Broccoli, A.J., Dahl, K.A. and Stouffer, R.J., 2006. Response of the ITCZ to Northern Hemisphere cooling. *Geophysical Research Letters*, *33*(1). doi:10.1029/2005GL024546

Burls, N.J., Fedorov, A.V., Sigman, D.M., Jaccard, S.L., Tiedemann, R. and Haug, G.H., 2017. Active Pacific meridional overturning circulation (PMOC) during the warm Pliocene. *Science advances*, *3*(9), p.e1700156. doi:10.1126/sciadv.1700156

Cai, W., Lengaigne, M., Borlace, S., Collins, M., Cowan, T., McPhaden, M.J., Timmermann, A., Power, S., Brown, J., Menkes, C. and Ngari, A., 2012. More extreme swings of the South Pacific convergence zone due to greenhouse warming. *Nature*, *488*(7411), pp. 365-369. doi:10.1038/nature11358

Calvert, S.E. and Pedersen, T.F., 2007. Chapter fourteen elemental proxies for palaeoclimatic and palaeoceanographic variability in marine sediments: interpretation and application. *Developments in Marine Geology*, *1*, pp. 567-644. doi:10.1016/S1572-5480(07)01019-6

Chappellaz, J., Barnola, J.M., Raynaud, D., Korotkevich, Y.S. and Lorius, C., 1990. Ice-core record of atmospheric methane over the past 160,000 years. *Nature*, *345*(6271), pp. 127-131. doi:10.1038/345127a0

Charles, S., Fu, G., Silberstein, R., Mpelasoka, F., McFarlane, D., Hogson, G., Teng, J., Gabrovesk, C., Ali, R., Barron, O., Aryal, A., and Dawes, W., 2015. Hydroclimate of the Pilbara: past, present and future. A report to the Government of Western Australia and industry partners from the CSIRO Pilbara Water Resource Assessment, CSIRO Land and Water, Australia., 114 pp. doi:10.4225/08/584af1c180bda

Cheng, H., Edwards, R.L., Broecker, W.S., Denton, G.H., Kong, X., Wang, Y., Zhang, R. and Wang, X., 2009. Ice age terminations. *science*, *326*(5950), pp. 248-252. doi:10.1126/science.1177840

Cheng, H., Edwards, R.L., Sinha, A., Spötl, C., Yi, L., Chen, S., Kelly, M., Kathayat, G., Wang, X., Li, X. and Kong, X., 2016. The Asian monsoon over the past 640,000 years and ice age terminations. *Nature*, *534*(7609), pp. 640-646. doi:10.1038/nature18591

Chiang, J.C. and Bitz, C.M., 2005. Influence of high latitude ice cover on the marine Intertropical Convergence Zone. *Climate Dynamics*, *25*(5), pp. 477-496. doi:10.1007/s00382-005-0040-5

Chiang, J.C., Biasutti, M. and Battisti, D.S., 2003. Sensitivity of the Atlantic intertropical convergence zone to last glacial maximum boundary conditions. *Paleoceanography*, *18*(4). doi:10.1029/2003PA000916

Chiang, J.C., Fang, Y. and Chang, P., 2008. Interhemispheric thermal gradient and tropical Pacific climate. *Geophysical Research Letters*, *35*(14). doi:10.1029/2008GL034166

Claussen, M., Brovkin, V., Ganopolski, A., Kubatzki, C. and Petoukhov, V., 2003. Climate change in northern Africa: The past is not the future. *Climatic Change*, *57*(1-2), pp. 99-118. doi:10.1023/A:1022115604225

De Deckker, P., 2001. Late Quaternary cyclic aridity in tropical Australia. *Palaeogeography, Palaeoclimatology, Palaeoecology*, *170*(1-2), pp. 1-9. doi:10.1016/S0031-0182(01)00233-4

De Deckker, P., Barrows, T.T. and Rogers, J., 2014. Land–sea correlations in the Australian region: post-glacial onset of the monsoon in northwestern Western Australia. *Quaternary Science Reviews*, *105*, pp. 181-194. doi:10.1016/j.quascirev.2014.09.030

De Deckker, P., Moros, M., Perner, K. and Jansen, E., 2012. Influence of the tropics and southern westerlies on glacial interhemispheric asymmetry. *Nature Geoscience*, *5*(4), pp.2 66-269. doi:10.1038/ngeo1431

Denniston, R.F., Ummenhofer, C.C., Wanamaker, A.D., Lachniet, M.S., Villarini, G., Asmerom, Y., Polyak, V.J., Passaro, K.J., Cugley, J., Woods, D. and Humphreys, W.F., 2016. Expansion and contraction of the Indo-Pacific tropical rain belt over the last three millennia. *Scientific Reports*, *6*(1), pp. 1-9. doi:10.1038/srep34485

Denniston, R.F., Asmerom, Y., Polyak, V.J., Wanamaker Jr, A.D., Ummenhofer, C.C., Humphreys, W.F., Cugley, J., Woods, D. and Lucker, S., 2017. Decoupling of monsoon activity across the northern and southern Indo-Pacific during the Late Glacial. *Quaternary Science Reviews*, 176, pp. 101-105. doi:10.1016/j.quascirev.2017.09.014

Denton, G.H., Anderson, R.F., Toggweiler, J.R., Edwards, R.L., Schaefer, J.M. and Putnam, A.E., 2010. The last glacial termination. *Science*, 328(5986), pp.1652-1656. doi:10.1126/science.1184119

DiNezio, P.N. and Tierney, J.E., 2013. The effect of sea level on glacial Indo-Pacific climate. *Nature Geoscience*, *6*(6), pp. 485-491. doi:10.1038/ngeo1823

Dykoski, C.A., Edwards, R.L., Cheng, H., Yuan, D., Cai, Y., Zhang, M., Lin, Y., Qing, J., An, Z. and Revenaugh, J., 2005. A high-resolution, absolute-dated Holocene and deglacial Asian monsoon record from Dongge Cave, China. *Earth and Planetary Science Letters*, *233*(1-2), pp. 71-86. doi:10.1016/j.epsl.2005.01.036

Frederiksen, C.S., Zheng, X. and Grainger, S., 2014. Teleconnections and predictive characteristics of Australian seasonal rainfall. *Climate dynamics*, *43*(5-6), pp.1381-1408. doi:10.1007/s00382-013-1952-0

Garbe-Schönberg, D. and Müller, S., 2014. Nano-particulate pressed powder tablets for LA-ICP-MS. *Journal of Analytical Atomic Spectrometry*, *29*(6), pp. 990-1000. doi:10.1039/C4JA00007B

Gingele, F.X. and De Deckker, P., 2004. Fingerprinting Australia's rivers with clay minerals and the application for the marine record of climate change. *Australian Journal of Earth Sciences*, *51*(3), pp. 339-348. doi:10.1111/j.1400-0952.2004.01061.x

Gingele, F.X., De Deckker, P. and Hillenbrand, C.D., 2001. Clay mineral distribution in surface sediments between Indonesia and NW Australia—source and transport by ocean currents. *Marine Geology*, *179*(3-4), pp. 135-146. doi:10.1016/S0025-3227(01)00194-3

Gonzalez-Muñoz, M.T., Martinez-Ruiz, F., Morcillo, F., Martin-Ramos, J.D. and Paytan, A., 2012. Precipitation of barite by marine bacteria: a possible mechanism for marine barite formation. *Geology*, *40*(8), pp. 675-678. doi:10.1130/G33006.1

Griffith, E.M. and Paytan, A., 2012. Barite in the ocean–occurrence, geochemistry and palaeoceanographic applications. *Sedimentology*, *59*(6), pp. 1817-1835. doi:10.1111/j.1365-3091.2012.01327.x

Griffiths, M.L., Drysdale, R.N., Gagan, M.K., Zhao, J.X., Ayliffe, L.K., Hellstrom, J.C., Hantoro, W.S., Frisia, S., Feng, Y.X., Cartwright, I. and Pierre, E.S., 2009. Increasing Australian–Indonesian monsoon rainfall linked to early Holocene sea-level rise. *Nature Geoscience*, *2*(9), pp. 636-639. doi:10.1038/ngeo605

Guo, Z., Zhou, X. and Wu, H., 2012. Glacial-interglacial water cycle, global monsoon and atmospheric methane changes. *Climate Dynamics*, *39*(5), pp. 1073-1092. doi:10.1007/s00382-011-1147-5

Hanebuth, T.J. and Henrich, R., 2009. Recurrent decadal-scale dust events over Holocene western Africa and their control on canyon turbidite activity (Mauritania). *Quaternary Science Reviews*, *28*(3-4), pp. 261-270. doi:10.1016/j.quascirev.2008.09.024

Haug, G.H., Hughen, K.A., Sigman, D.M., Peterson, L.C. and Röhl, U., 2001. Southward migration of the intertropical convergence zone through the Holocene. *Science*, *293*(5533), pp. 1304-1308. doi:10.1126/science.1059725

Heirtzler, J.R., 1974. Aeolian transport of dust off western Australia: in Veevers, J. J., J. R. Heirtzler et al., Initial reports of the Deep Sea Drilling Project: v. 27 (U. S. Government Printing Office), Washington, p. 397-399.

Henrich, R., Hanebuth, T.J.J., Cherubini, Y., Krastel, S., Pierau, R. and Zühlsdorf, C., 2010. Climate-induced turbidity current activity in NW-African canyon systems. In *Submarine mass movements and their consequences* (pp. 447-459). Springer, Dordrecht. doi:10.1016/j.jop.2015.08.011

Hesse, P.P., Magee, J.W. and van der Kaars, S., 2004. Late Quaternary climates of the Australian arid zone: a review. *Quaternary International*, *118*, pp. 87-102. doi:10.1016/S1040-6182(03)00132-0

Hesse, P.P. and McTainsh, G.H., 2003. Australian dust deposits: modern processes and the Quaternary record. *Quaternary Science Reviews*, *22*(18-19), pp.2007-2035. doi:10.1016/S0277-3791(03)00164-1

Holbourn, A., Kuhnt, W., Kawamura, H., Jian, Z., Grootes, P., Erlenkeuser, H. and Xu, J., 2005. Orbitally paced paleoproductivity variations in the Timor Sea and Indonesian Throughflow variability during the last 460 kyr. *Paleoceanography*, *20*(3). doi:10.1029/2004PA001094

Jansen, J.H.F., Kuijpers, A. and Troelstra, S.R., 1986. A mid-Brunhes climatic event: Long-term changes in global atmosphere and ocean circulation. *Science*, *232*(4750), pp. 619-622. doi:10.1126/science.232.4750.619

Jansen, J.H.F., Van der Gaast, S.J., Koster, B. and Vaars, A.J., 1998. CORTEX, a shipboard XRF-scanner for element analyses in split sediment cores. *Marine Geology*, *151*(1-4), pp. 143-153. doi:10.1016/S0025-3227(98)00074-7

Jickells, T.D., An, Z.S., Andersen, K.K., Baker, A.R., Bergametti, G., Brooks, N., Cao, J.J., Boyd, P.W., Duce, R.A., Hunter, K.A. and Kawahata, H., 2005. Global iron connections between desert dust, ocean biogeochemistry, and climate. *Science*, *308*(5718), pp. 67-71. doi:10.1126/science.1105959

Kathayat, G., Cheng, H., Sinha, A., Spötl, C., Edwards, R.L., Zhang, H., Li, X., Yi, L., Ning, Y., Cai, Y. and Lui, W.L., 2016. Indian monsoon variability on millennial-orbital timescales. *Scientific reports*, *6*, p.24374. doi:10.1038/srep24374

Kawamura, H., Holbourn, A. and Kuhnt, W., 2006. Climate variability and land–ocean interactions in the Indo Pacific Warm Pool: a 460-ka palynological and organic geochemical record from the Timor Sea. *Marine Micropaleontology*, *59*(1), pp. 1-14. doi:10.1016/j.marmicro.2005.09.001

Keep, M., Holbourn, A., Kuhnt, W. and Gallagher, S.J., 2018. Progressive Western Australian collision with Asia: implications for regional orography, oceanography, climate and marine biota. *Journal of the Royal Society of Western Australia*, *101*, pp. 1-16.

Kelly, M.J., Edwards, R.L., Cheng, H., Yuan, D., Cai, Y., Zhang, M., Lin, Y. and An, Z., 2006. High resolution characterization of the Asian Monsoon between 146,000 and 99,000 years BP from Dongge Cave, China and global correlation of events surrounding Termination II. *Palaeogeography, Palaeoclimatology, Palaeoecology*, *236*(1-2), pp. 20-38. doi:10.1016/j.palaeo.2005.11.042

Kershaw, A.P., van der Kaars, S. and Moss, P.T., 2003. Late Quaternary Milankovitch-scale climatic change and variability and its impact on monsoonal Australasia. *Marine Geology*, *201*(1-3), pp. 81-95. doi:10.1016/S0025-3227(03)00210-X

Kuhnt, W., Holbourn, A., Xu, J., Opdyke, B., De Deckker, P., Röhl, U. and Mudelsee, M., 2015. Southern Hemisphere control on Australian monsoon variability during the late deglaciation and Holocene. *Nature communications*, *6*(1), pp. 1-7. doi:10.1038/ncomms8916

Kuhnt, W., Holbourn, A., Schönfeld, J., Lindhorst, K., Gallagher, S., Keep, M., Sadekov, A., Dunlea, A., Clemens, S., Wilkens, R., Sarnthein, M., Leutert, T., Zhang, P., Maicher, D., Manceau, R., Dillon, A., Gonzalez, J.-L., Fabian, S., McCaffrey, J., Kochhann, K., Lübbers, J., Jöhnck, J., Hingst, J., Parplies, K., Koppe, M., Steffen, S., Schultz, J., Heinrich, S., Averes, T. and Evers, F., 2018. Cruise Report Sonne 257, WACHEIO - Western Australian Climate History from Eastern Indian Ocean Sediment Archives, Darwin - Fremantle, May 12, 2017 - June 04, 2017. Institut für Geowissenschaften, Christian-Albrechts-Universität Kiel, 260 pp. doi:10.2312/cr_so257

Lauterbach, S., Andersen, N., Wang, Y. V., Blanz, T., Larsen, T., & Schneider, R. R. (2020). An ~130 kyr record of surface water temperature and $\delta^{18}O$ from the northern Bay of Bengal: Investigating the linkage between Heinrich events and Weak Monsoon Intervals in Asia. Paleoceanography and Paleoclimatology, 35, e2019PA003646. doi:10.1029/2019PA003646

Lechler, P.J. and Desilets, M.O., 1987. A review of the use of loss on ignition as a measurement of total volatiles in whole-rock analysis. *Chemical Geology*, *63*(3-4), pp. 341-344. doi:10.1016/0009-2541(87)90171-9

Lisiecki, L.E. and Raymo, M.E., 2005. A Pliocene-Pleistocene stack of 57 globally distributed benthic δ18O records. *Paleoceanography*, *20*(1). doi:10.1029/2004PA001071

Liu, L., Chen, J., Chen, Y., Ji, J. and Lu, H., 2002. Variation of Zr/Rb ratios on the Loess Plateau of Central China during the last 130000 years and its implications for winter monsoon. *Chinese Science Bulletin*, *47*(15), pp. 1298-1302. doi:10.1360/02tb9288

Liu, Z., Wen, X., Brady, E.C., Otto-Bliesner, B., Yu, G., Lu, H., Cheng, H., Wang, Y., Zheng, W., Ding, Y. and Edwards, R.L., 2014. Chinese cave records and the East Asia summer monsoon. *Quaternary Science Reviews*, *83*, pp. 115-128. doi:10.1016/j.quascirev.2013.10.021

Loulergue, L., Schilt, A., Spahni, R., Masson-Delmotte, V., Blunier, T., Lemieux, B., Barnola, J.M., Raynaud, D., Stocker, T.F. and Chappellaz, J., 2008. Orbital and millennial-scale features of atmospheric CH 4 over the past 800,000 years. *Nature*, *453*(7193), pp. 383-386. doi:10.1038/nature06950

Lu, J., Vecchi, G.A. and Reichler, T., 2007. Expansion of the Hadley cell under global warming. *Geophysical Research Letters*, *34*(6). doi:10.1029/2006GL028443

Lüthi, D., Le Floch, M., Bereiter, B., Blunier, T., Barnola, J. M., Siegenthaler, D., Raynaud, J., Jouzel, H., Fischer, K., Kawamura and Stocker, T. F., 2008. High-resolution carbon dioxide concentration record 650,000–800,000 years before present. *Nature*, *453*(7193), pp. 379-382. doi:10.1038/nature06949

Lübbers, J., Kuhnt, W., Holbourn, A.E., Bolton, C.T., Gray, E., Usui, Y., Kochhann, K.G., Beil, S. and Andersen, N., 2019. The middle to late Miocene "Carbonate Crash" in the equatorial Indian Ocean. *Paleoceanography and Paleoclimatology*, *34*(5), pp. 813-832. doi:10.1029/2018PA003482

McTainsh, G.H., 1989. Quaternary aeolian dust processes and sediments in the Australian region. *Quaternary Science Reviews*, *8*(3), pp. 235-253. doi:10.1016/0277-3791(89)90039-5

Mohtadi, M., Oppo, D.W., Steinke, S., Stuut, J.B.W., De Pol-Holz, R., Hebbeln, D. and Lückge, A., 2011. Glacial to Holocene swings of the Australian–Indonesian monsoon. *Nature Geoscience*, *4*(8), pp. 540-544. doi:10.1038/ngeo1209

Mohtadi, M., Prange, M. and Steinke, S., 2016. Palaeoclimatic insights into forcing and response of monsoon rainfall. *Nature*, *533*(7602), pp. 191-199. doi:10.1038/nature17450

Muller, J., Kylander, M., Martinez-Cortizas, A., Wüst, R.A., Weiss, D., Blake, K., Coles, B. and Garcia-Sanchez, R., 2008. The use of principle component analyses in characterising trace and major elemental distribution in a 55 kyr peat deposit in tropical Australia: implications to paleoclimate. *Geochimica et Cosmochimica Acta*, *72*(2), pp. 449-463. doi:10.1016/j.gca.2007.09.028

Muller, J., Kylander, M., Wüst, R.A., Weiss, D., Martinez-Cortizas, A., LeGrande, A.N., Jennerjahn, T., Behling, H., Anderson, W.T. and Jacobson, G., 2008. Possible evidence for wet Heinrich phases in tropical NE Australia: the Lynch's Crater deposit. *Quaternary Science Reviews*, *27*(5-6), pp. 468-475. doi:10.1016/j.quascirev.2007.11.006

Muller, J., McManus, J.F., Oppo, D.W. and Francois, R., 2012. Strengthening of the Northeast Monsoon over the Flores Sea, Indonesia, at the time of Heinrich event 1. *Geology*, *40*(7), pp. 635-638. doi:10.1130/G32878.1

Paillard, D., Labeyrie, L. and Yiou, P., 1996. Macintosh program performs time-series analysis. *Eos, Transactions American Geophysical Union*, *77*(39), pp. 379-379. doi:10.1029/96EO00259

Partin, J.W., Cobb, K.M., Adkins, J.F., Clark, B. and Fernandez, D.P., 2007. Millennial-scale trends in west Pacific warm pool hydrology since the Last Glacial Maximum. *Nature*, *449*(7161), pp. 452-455. doi:10.1038/nature06164

Poulton, S.W., Raiswell, R., 2002. The low-temperature geochemical cycle of iron: From continental fluxes to marine sediment deposition. Am. J. Sci. 302, 774–805. doi:10.2475/ajs.302.9.774

Pusey, B.J. and Kath, J., 2015. Environmental Water Management in the Fitzroy River Valley Information availability, knowledge gaps and research needs. *Unpublished report to the Department of Water, Western Australia*. doi:10.13140/RG.2.1.3739.4966

Rea, D.K., 1994. The paleoclimatic record provided by eolian deposition in the deep sea: The geologic history of wind. *Reviews of Geophysics*, *32*(2), pp. 159-195. doi:10.1029/93RG03257

Revill, A.T., Jones, N.L., Hipsey, M.J., Bruce, L.C., Silberstein, R.P., Furnas, M., Donn, M., Espinosa, A., Gruber, R. and Zhou, W., 2017. Terrestrial-Ocean Linkages: the role of rivers and estuaries in sustaining marine productivity in the Kimberley. *Report of Project*, *2*(6).

Rhodes, R.H., Brook, E.J., Chiang, J.H.C., Bunier, T., Maselli, O.J., McConnell, J.R., Romanini, J.R., and Severinghaus, J.P., 2015. Enhanced tropical methane production in response to iceberg discharge in the North Atlantic. Science 348/6238, pp. 1016-1019, doi:10.1126/science.1262005

Risbey, J.S., Pook, M.J., McIntosh, P.C., Wheeler, M.C. and Hendon, H.H., 2009. On the remote drivers of rainfall variability in Australia. *Monthly Weather Review*, *137*(10), pp. 3233-3253. doi:10.1175/2009MWR2861.1

Rosenthal, Y., Holbourn, A.E. and Kulhanek, D.K., and the Expedition 363 Scientists, 2017. Expedition 363 Preliminary Report: Western Pacific Warm Pool. International Ocean Discovery Program. pp. 11-13. doi:10.14379/iodp.pr.363.2017

Rosenthal, Y., Holbourn, A.E., Kulhanek, D.K., and the Expedition 363 Scientists, 2018. *Western Pacific Warm Pool.* Proceedings of the International Ocean Discovery Program, 363: College Station, TX (International Ocean Discovery Program). doi:10.14379/iodp.proc.363.2018

Rosenthal, Y., Oppo, D.W. and Linsley, B.K., 2003. The amplitude and phasing of climate change during the last deglaciation in the Sulu Sea, western equatorial Pacific. *Geophysical Research Letters*, *30*(8). doi:10.1029/2002GL016612

Sarnthein, M., Grootes, P.M., Holbourn, A., Kuhnt, W. and Kühn, H., 2011. Tropical warming in the Timor Sea led deglacial Antarctic warming and atmospheric CO2 rise by more than 500 yr. *Earth and Planetary Science Letters*, *302*(3-4), pp. 337-348. doi:10.1016/j.epsl.2010.12.021

Schneider, T., Bischoff, T. and Haug, G.H., 2014. Migrations and dynamics of the intertropical convergence zone. *Nature*, *513*(7516), pp. 45-53. doi:10.1038/nature13636

Schröder, J.F., Holbourn, A., Kuhnt, W. and Küssner, K., 2016. Variations in sea surface hydrology in the southern Makassar Strait over the past 26 kyr. *Quaternary Science Reviews*, *154*, pp. 143-156. doi:10.1016/j.quascirev.2016.10.018

Schröder, J.F., Kuhnt, W., Holbourn, A., Beil, S., Zhang, P., Hendrizan, M. and Xu, J., 2018. Deglacial warming and hydroclimate variability in the central Indonesian Archipelago. *Paleoceanography and Paleoclimatology*, *33*(9), pp.974-993. doi:10.1029/2018PA003323

Seidel, D. J., Fu, Q., Randel, W. J. & Reichler, T. J., 2008. Widening of the tropical belt in a changing climate. Nature Geosciences 1, 21–24.

Shakun, J.D., Clark, P.U., He, F., Marcott, S.A., Mix, A.C., Liu, Z., Otto-Bliesner, B., Schmittner, A. and Bard, E., 2012. Global warming preceded by increasing carbon dioxide concentrations during the last deglaciation. *Nature*, *484*(7392), pp. 49-54. doi:10.1038/nature10915

Sniderman, J.K., Brown, J.R., Woodhead, J.D., King, A.D., Gillett, N.P., Tokarska, K.B., Lorbacher, K., Hellstrom, J., Drysdale, R.N. and Meinshausen, M., 2019. Southern Hemisphere subtropical drying as a transient response to warming. *Nature Climate Change*, *9*(3), pp. 232-236. doi:10.1038/s41558-019-0397-9

Stager, J.C., Ryves, D.B., Chase, B.M. and Pausata, F.S., 2011. Catastrophic drought in the Afro-Asian monsoon region during Heinrich event 1. *Science*, *331*(6022), pp. 1299-1302. doi:10.1126/science.1198322

Stríkis, N.M., Cruz, F.W., Barreto, E.A., Naughton, F., Vuille, M., Cheng, H., Voelker, A.H., Zhang, H., Karmann, I., Edwards, R.L. and Auler, A.S., 2018. South American monsoon response to iceberg discharge in the North

Atlantic. *Proceedings of the National Academy of Sciences*, *115*(15), pp. 3788-3793. doi:10.1073/pnas.1717784115

Stuiver, M., Reimer, P.J. and Reimer, R.W., 2019. Calib Radiocarbon calibration 7.0. *World Wide Web: http://calib. qub. ac. uk/calib/. Accessed*, *1*.

Stuut, J.B.W., Temmesfeld, F. and De Deckker, P., 2014. A 550 ka record of aeolian activity near North West Cape, Australia: inferences from grain-size distributions and bulk chemistry of SE Indian Ocean deep-sea sediments. *Quaternary Science Reviews*, *83*, pp. 83-94. doi:10.1016/j.quascirev.2013.11.003.

Sudmeyer, R., 2016. Climate in the Pilbara, Bulletin 4873, Department of Agriculture and Food, Western Australia, Perth, 46 pp.

Suppiah, R., 1992. The Australian summer monsoon: a review. *Progress in Physical Geography*, *16*(3), pp.283-318. doi:10.1177/030913339201600302

Taylor, S.R. and McLennan, S.M., 1985. The continental crust: its composition and evolution. Blackwell Scientific, Oxford, 312 pp.

Tjallingii, R., Röhl, U., Kölling, M. and Bickert, T., 2007. Influence of the water content on X-ray fluorescence core-scanning measurements in soft marine sediments. *Geochemistry, Geophysics, Geosystems*, *8*(2). doi:10.1029/2006GC001393

Thirumalai, K., Clemens, S.C. and Partin, J.W., 2020. Methane, Monsoons, and Modulation of Millennial-Scale Climate. *Geophysical Research Letters*, *47*(9), p.e2020GL087613. doi:10.1029/2020GL087613

Tory, K.J., Dare, R.A., 2015. Sea surface temperature thresholds for tropical cyclone formation. J. Clim. 28, 8171–8183. doi:10.1175/JCLI-D-14-00637.1

Turekian, K.K. and Wedepohl, K.H., 1961. Distribution of the elements in some major units of the earth's crust. *Geological Society of America Bulletin*, *72*(2), pp. 175-192. doi:10.1130/0016-7606(1961)72[175:DOTEIS]2.0.CO;2

Turney, C.S., Haberle, S., Fink, D., Kershaw, A.P., Barbetti, M., Barrows, T.T., Black, M., Cohen, T.J., Correge, T., Hesse, P.P. and Hua, Q., 2006. Integration of ice-core, marine and terrestrial records for the Australian Last Glacial Maximum and Termination: a contribution from the OZ INTIMATE group. *Journal of Quaternary Science: Published for the Quaternary Research Association*, *21*(7), pp. 751-761. doi:10.1002/jqs.1073

Vogel, W. and Kuipers, G., 1987. A pre-calibrated program for geological applications, Phillips New Developments. *X-Ray Spectrometry.*, *11*, pp. 2-8.

Wang, Y.J., Cheng, H., Edwards, R.L., An, Z.S., Wu, J.Y., Shen, C.C. and Dorale, J.A., 2001. A high-resolution absolute-dated late Pleistocene monsoon record from Hulu Cave, China. Science, 294(5550), pp. 2345-2348. doi:10.1126/science.1064618

Wang, Y., Cheng, H., Edwards, R.L., Kong, X., Shao, X., Chen, S., Wu, J., Jiang, X., Wang, X. and An, Z., 2008. Millennial-and orbital-scale changes in the East Asian monsoon over the past 224,000 years. *Nature*, *451*(7182), pp. 1090-1093. doi:10.1038/nature06692

Webster, P.J., Magana, V.O., Palmer, T.N., Shukla, J., Tomas, R.A., Yanai, M.U. and Yasunari, T., 1998. Monsoons: Processes, predictability, and the prospects for prediction. *Journal of Geophysical Research: Oceans*, *103*(C7), pp. 14451-14510.doi:10.1029/97JC02719

Wedepohl, K., 1971. Geochemistry: Holt. *Rinehart and Winston, New York.*, *231 pp*

Weltje, G.J. and Tjallingii, R., 2008. Calibration of XRF core scanners for quantitative geochemical logging of sediment cores: Theory and application. *Earth and Planetary Science Letters*, *274*(3-4), pp. 423-438. doi:10.1016/j.epsl.2008.07.054

Wyrwoll, K.H., Liu, Z., Chen, G., Kutzbach, J.E. and Liu, X., 2007. Sensitivity of the Australian summer monsoon to tilt and precession forcing. *Quaternary Science Reviews*, *26*(25-28), pp. 3043-3057. doi:10.1016/j.quascirev.2007.06.026

Yuan, D., Cheng, H., Edwards, R.L., Dykoski, C.A., Kelly, M.J., Zhang, M., Qing, J., Lin, Y., Wang, Y., Wu, J. and Dorale, J.A., 2004. Timing, duration, and transitions of the last interglacial Asian monsoon. *Science*, *304*(5670), pp. 575-578. doi:10.1126/science.1091220

Zhang, P., Xu, J., Holbourn, A., Kuhnt, W., Beil, S., Li, T., Xiong, Z., Dang, H., Yan, H., Pei, R. and Ran, Y., 2020 (in press). Indo-Pacific hydroclimate in response to changes of the Intertropical Convergence Zone: Discrepancy on precession and obliquity bands over the last 410 kyr. *Journal of Geophysical Research: Atmospheres*, p.e2019JD032125. doi:10.1029/2019JD032125

Figure 1. A. Main rivers discharging sediment to the northwestern Australian margin and average Holocene-MIS-6 sedimentation rates (cm/kyr) along the margin. Water depth scale in m. **B.** Summer monsoonal (February) vegetation and precipitation patterns. Average sedimentation rates (cm/kyr) are from Sonne 257 cores offshore Australia (from Keep et al., 2018; Kuhnt et al., 2018). February precipitation is based on 30 yr standard climatology (1961-1990) in mm/month from Australian Bureau of Meteorology (2010). Satellite Image is from February 2004 from NASA Blue Marble.

Figure 2. Location of Cores SO257-18548 and -18571 and IODP Site U1482 offshore northwestern Australia (A). Base map created using www.maps-for-free.com. Detailed maps (B-C) show positions of coring sites in relation to

adjacent main rivers and concentrations of main terrigenous elements (Si, Al, Fe, K and Ti)) in fine-grained (<63 μm) fractions of terrigenous material in marine sediment cores (B) and river sediments (C). Approximate extension of glacial Fitzroy River on shelf is indicated by blue dashed line in B.

Figure 3. Correlation of benthic foraminiferal $\delta^{18}O$ from Core SO257-18548 and Site U1482 to benthic isotope stack LR04 (Lisiecki and Raymo, 2005). Dashed black lines indicate tie points used to derive age model. Dashed red lines indicate AMS^{14}C ages. Orange dashed lines indicate biostratigraphic datums: B = Base, T = Top (from Rosenthal et al., 2018).

Figure 4. Correlation of benthic foraminiferal $\delta^{18}O$ of Core SO257-18571 to the benthic isotope stack LR04 (Lisiecki and Raymo, 2005). Dashed black lines indicate tie points used to derive age model. Dashed red lines indicate AMS^{14}C ages.

Figure 5. Temporal evolution of XRF scanner derived elemental ratios and benthic foraminiferal $\delta^{18}O$. MIS = marine isotope stages.（A-B) Log(Zr/Rb) from Core SO257-18548 and Site U1482 (orange) and from Core SO257-18571 (red); (C-D) Log(Terr/Ca) from Core SO257-18548 and Site U1482(black) and from Core SO257-18571 (purple); (E-F) benthic $\delta^{18}O$ from SO257-18548 and Site U1482 (dark blue) and from Core SO257-18571 (light blue). Blue shading indicates marine isotope glacial stages (MIS), following Lisiecki and Raymo (2005).

Figure 6. Comparison of monsoonal discharge (Log(Terr/Ca)) in composite record from Core SO157-18548 and Site U1482 with evolution of Antarctic temperatures (Epica Dome Concordia (EDC) δD from Bazin et al., 2013) and Northern Hemisphere monsoon intensity (Chinese speleothem $\delta^{18}O$ record from Dongge, Hulu and Sanbao Caves. Wang et al., 2001,2008; Dykoski et al., 2005; Kelly et al., 2006; Cheng et al., 2009, 2016). Note that monsoonal discharge record is tuned to LR04 stack (Lisiecki and Raymo, 2005) and, thus, independent of EDC ice core age model. Glacial Terminations I-V in LR04 stack are marked with blue (onset) and red (end) dashed lines; corresponding ages are 18-9 ka (Termination I), 135-126 ka (Termination II), 252-240 ka (Termination III), 341-329 ka (Terminations IV) and 431-410 ka (Termination V).

Figure 7. Comparison of terrigenous discharge records from Cores SO257-18571, SO257-18548 and Site U1482 to external and internal forcing mechanisms. (A) Insolation 21st of September at 20°S; (B) Insolation gradient between 10 and 30°S; (C) Log(Terr/Ca) from Core SO257-18548 and Site U1482 (black); (D) Log(Terr/Ca) from Core SO257-18571 (purple); (E) EPICA Dome Concordia (EDC) CH_4 record (Loulergue et al., 2008); (F) EDC CO_2 record (Lüthi. et al., 2008.). Green shading marks monsoonal peaks associated with pCO_2 maxima occurring at austral spring insolation maxima and minimal gradient between 10 and 30° S insolation, which favors southward migration of the ITCZ.

Table 1. AMS ^{14}C dates from analysis of *Globigerinoides ruber* (white)

Kiel AMS Laboratory Number	Core	Depth (cm)	Foraminiferal species	Uncorr. ^{14}C Age (years B.P.)	Error bar	Reservoir Age (years)	Calibrated Age (years B.P.)

KIA 53786	SO257-18548	70	*G. ruber*	11765	45	510	13114
KIA 53787	SO257-18548	100	*G. ruber*	18305	70	1600	20154
KIA 53788	SO257-18571	140	*G. ruber*	9980	40	250	10738
KIA 53789	SO257-18571	190	*G. ruber*	18830	75	1600	20778

Table 2. Age tie points to LR04 benthic isotope stack (Lisiecki and Raymo, 2005)

SO257-18548 and U1482		SO257-18571			
Core Depth (m)	$\delta^{18}O$ (‰ VPDB)	Core Depth (m)	$\delta^{18}O$ (‰ VPDB)	Age (ka)	Description of tie points
2.7	3.68	3.6	3.3	62	$\delta^{18}O$ maximum in center of MIS 4
3.7	3.11	5.1	3.05	87	$\delta^{18}O$ maximum in center of MIS 5b
4.4	3.11	6.9	3.07	109	$\delta^{18}O$ maximum in center of MIS 5d
5.1	3.76	9.2	3.6	135	Onset of Termination II
6.5	3.4	11.1	3.12	183	Onset of MIS 6
7.6	3.49	14.4	3.3	223	Onset of Termination IIIb
8.4	3.56	16.2	3.17	252	Onset of Termination IIIa
9	3.49	16.9	3.1	277	Onset of second $\delta^{18}O$ maximum in MIS 8
9.7	3.38	17.7	2.9	294	First $\delta^{18}O$ maximum in MIS 8
10.5	2.86	19.3	2.43	318	End of first $\delta^{18}O$ minimum in MIS 9
11.7	3.73			342	Onset of Termination IV
13.9	3.3			392	End of first $\delta^{18}O$ minimum in MIS 11
15.5	3.8			433	Onset of Termination V

Table 3. Concentration of main terrigenous elements in Cores SO257-18548 and -18571 and close by rivers. Fitz = Fitzroy River, Ashb = Ashburton River, Fort = Fortescue River, Gasc = Gascoyne River

Elements	**18548 (%)**	Derby (%)	Fitz1 (%)	Fitz2 (%)	**18571 (%)**	Ashb1 (%)	Fort1 (%)	Fort2 (%)	Gasc1 (%)	Gasc2 (%)
Si	**65.72**	60.28	79.67	77.34	**67.37**	68.84	66.08	65.63	63.18	66.38
Al	**21.75**	24.35	11.81	13.19	**19.72**	15.69	14.15	14.27	22.10	19.26
Fe	**8.56**	10.90	5.25	6.04	**9.30**	12.03	16.85	17.27	11.08	10.44
K	**3.06**	3.44	2.05	2.39	**2.37**	2.33	1.72	1.71	2.50	2.43
Ti	**0.90**	1.03	1.22	1.03	**1.24**	1.10	1.21	1.12	1.14	1.50

Key findings

- Rapid intensification of Australian monsoon at end of glacial terminations I to IV

- Monsoon intensification coincided with atmospheric CO_2 increase
- Austral spring insolation drove southward shift of ITCZ and monsoon intensification
- Formation of regional heat lows instrumental for monsoonal hydroclimate
- Aeolian dust dominant during glacials and MIS 5a-d south of 20°S.

Figure 1

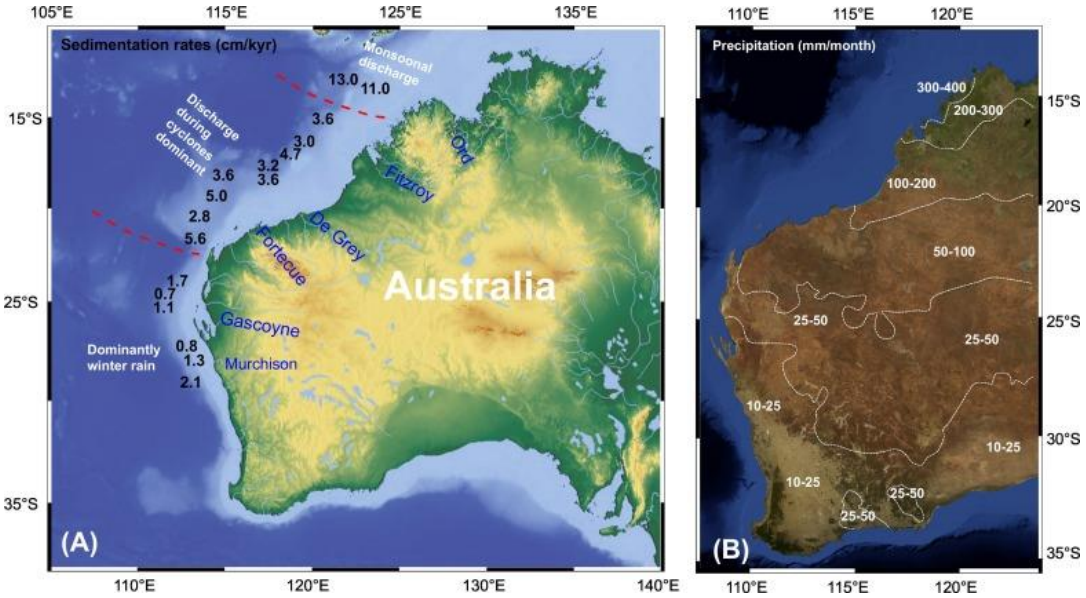

Figure 2

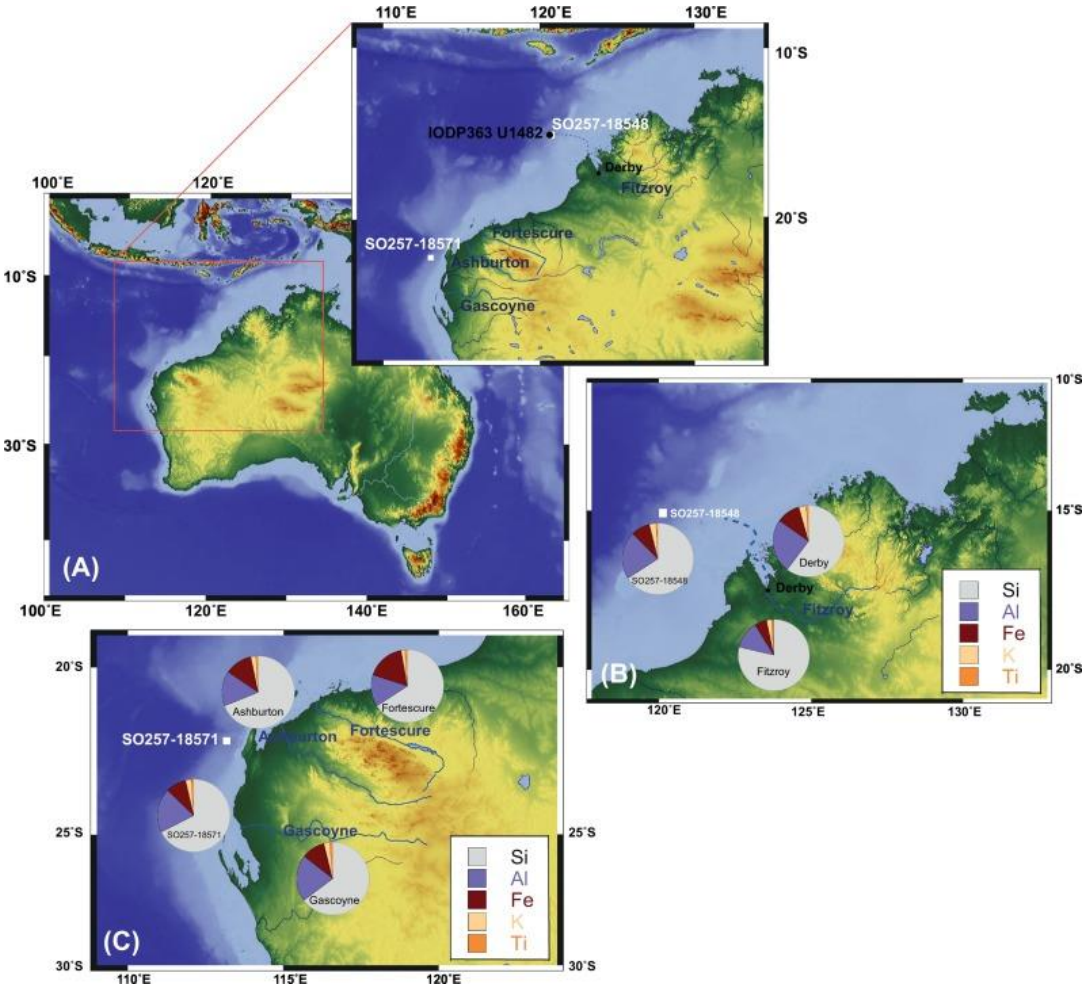

Figure 3

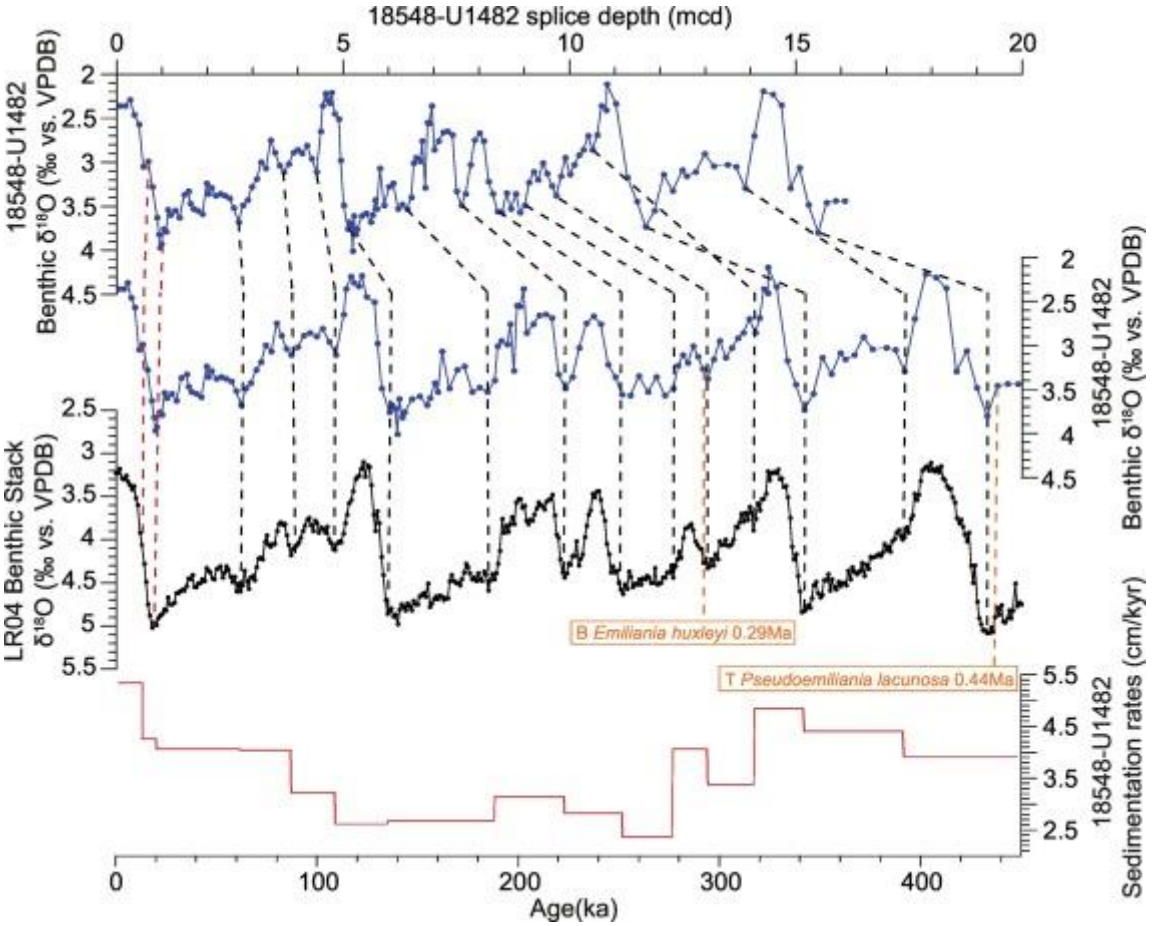
18548-U1482 splice depth (mcd)
0
5
10
15
20
18548-U1482
Benthic δ18O (‰ vs. VPDB)
2
2.5
3
3.5
4
4.5
LR04 Benthic Stack
δ18O (‰ vs. VPDB)
2.5
3
3.5
4
4.5
5
5.5
B Emiliania huxleyi 0.29Ma
T Pseudoemiliania lacunosa 0.44Ma
18548-U1482
Benthic δ18O (‰ vs. VPDB)
18548-U1482
Sedimentation rates (cm/kyr)
5.5
4.5
3.5
2.5
0
100
200
300
400
Age(ka)

Figure 4

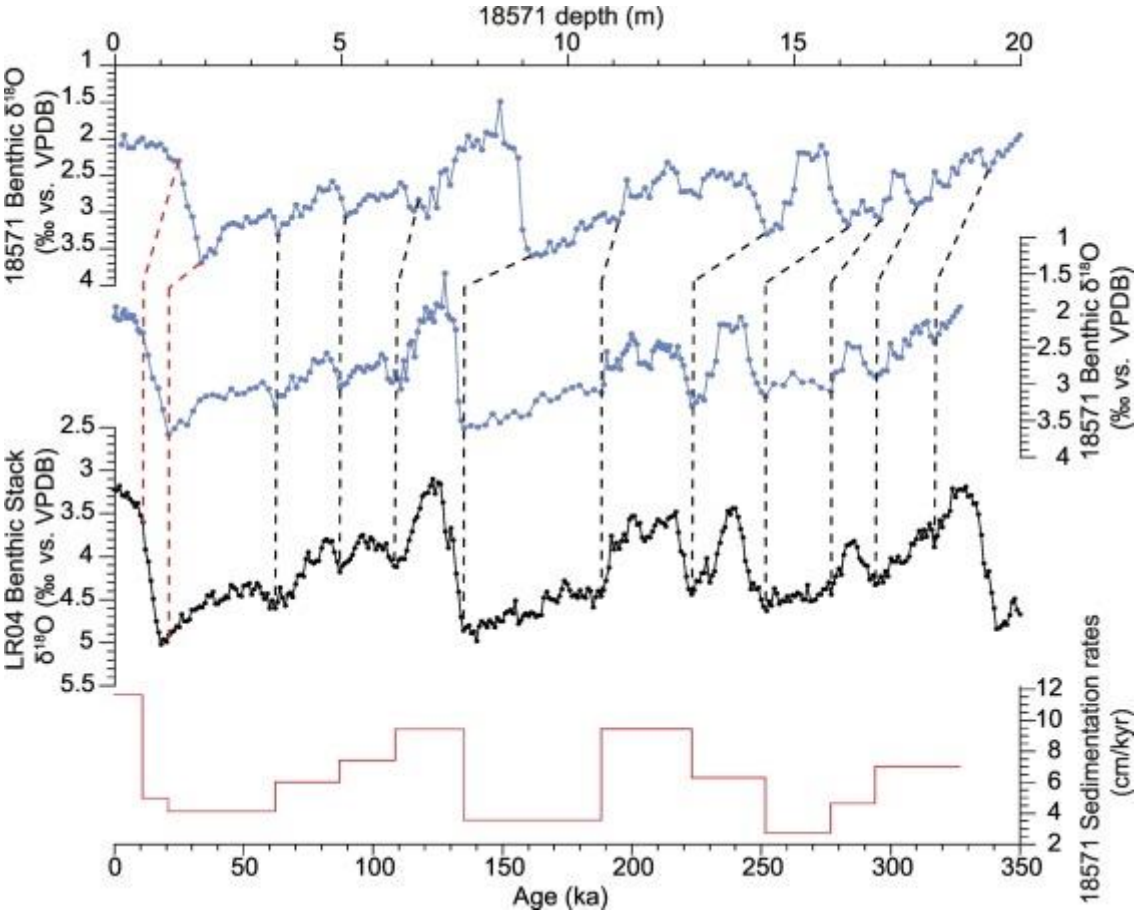
18571 depth (m)
0
5
10
15
20
18571 Benthic δ18O (‰ vs. VPDB)
1
1.5
2
2.5
3
3.5
4
LR04 Benthic Stack δ18O (‰ vs. VPDB)
2.5
3
3.5
4
4.5
5
5.5
18571 Benthic δ18O (‰ vs. VPDB)
18571 Sedimentation rates (cm/kyr)
12
10
8
6
4
2
0
50
100
150
200
250
300
350
Age (ka)

Figure 5

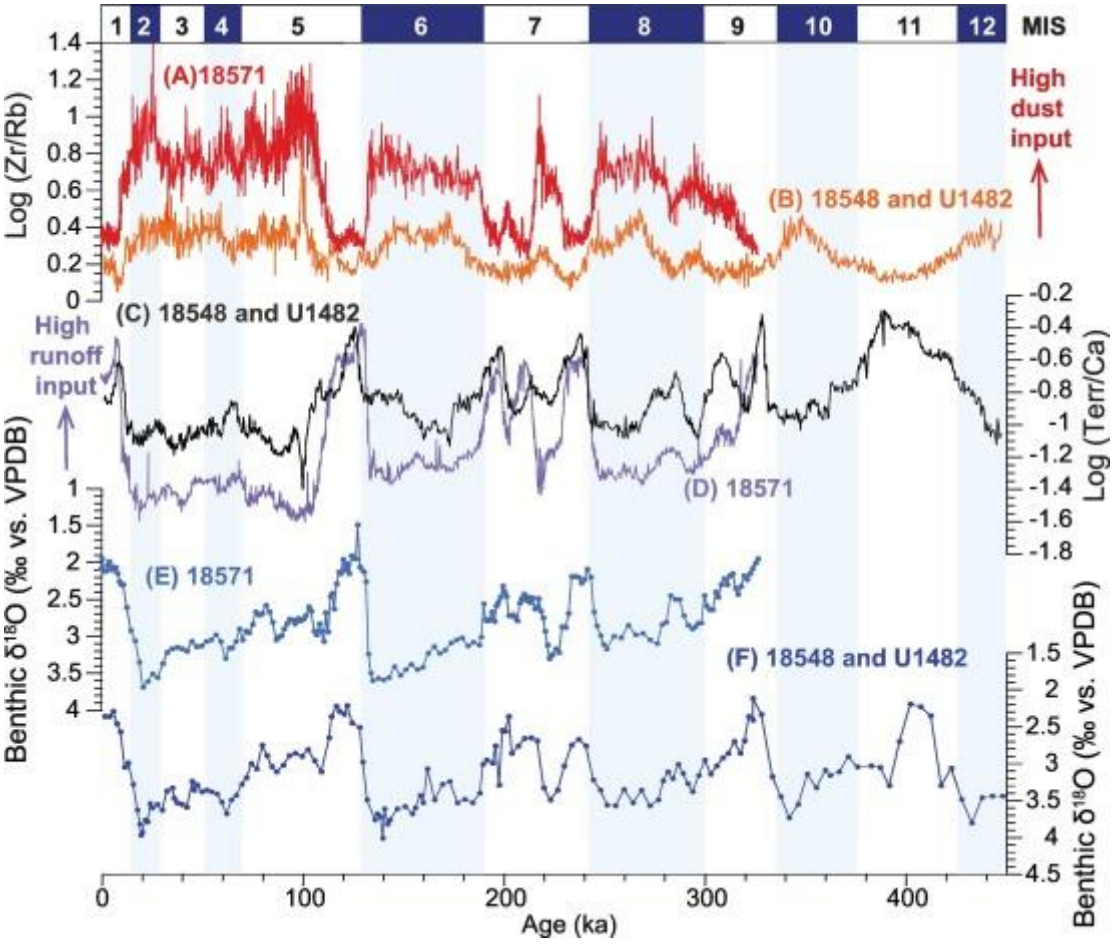
1
2
3
4
5
6
7
8
9
10
11
12
MIS
(A)18571
High dust input
(B) 18548 and U1482
Log (Zr/Rb)
(C) 18548 and U1482
High runoff input
(D) 18571
Log (Terr/Ca)
(E) 18571
(F) 18548 and U1482
Benthic δ18O (‰ vs. VPDB)
Age (ka)

Figure 6

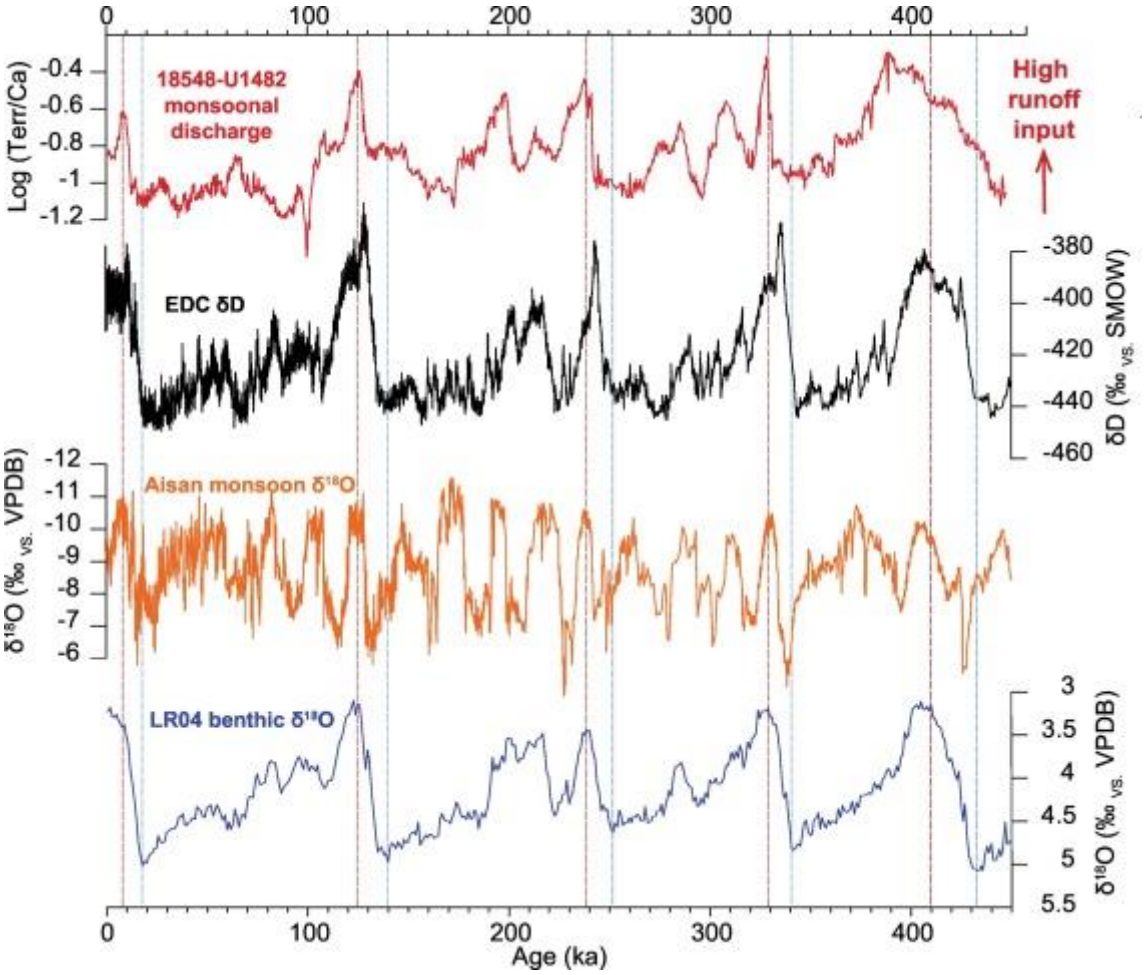
0
100
200
300
400
18548-U1482
monsoonal
discharge
High
runoff
input
Log (Terr/Ca)
-0.4
-0.6
-0.8
-1
-1.2
EDC δD
-380
-400
-420
-440
-460
δD (‰ vs. SMOW)
Aisan monsoon δ18O
δ18O (‰ vs. VPDB)
-12
-11
-10
-9
-8
-7
-6
LR04 benthic δ18O
3
3.5
4
4.5
5
5.5
δ18O (‰ vs. VPDB)
Age (ka)

Figure 7

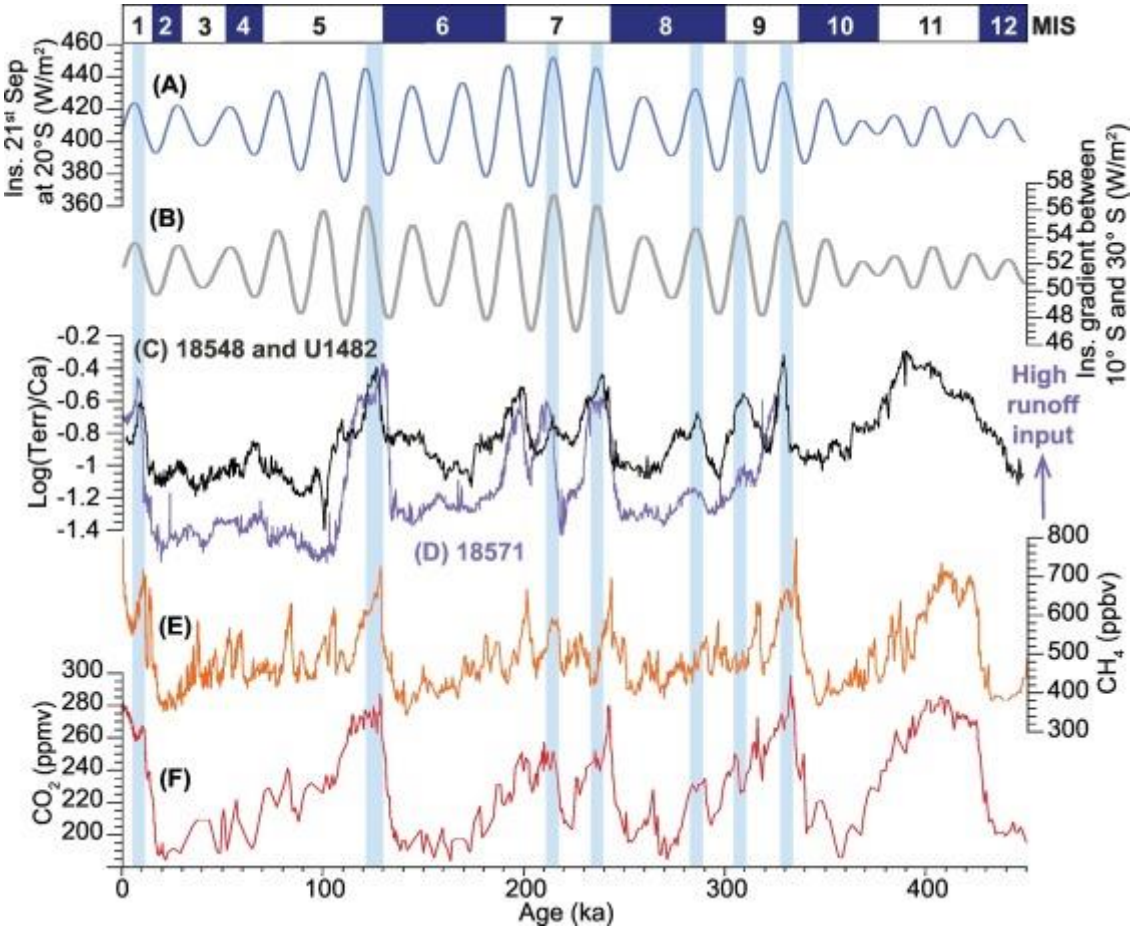
1
2
3
4
5
6
7
8
9
10
11
12
MIS
Ins. 21st Sep at 20°S (W/m²)
460
440
420
400
380
360
(A)
(B)
Ins. gradient between 10° S and 30° S (W/m²)
58
56
54
52
50
48
46
(C) 18548 and U1482
Log(Terr)/Ca)
-0.2
-0.4
-0.6
-0.8
-1
-1.2
-1.4
High runoff input
(D) 18571
800
700
600
500
400
300
CH4 (ppbv)
(E)
300
280
260
240
220
200
CO2 (ppmv)
(F)
0
100
200
300
400
Age (ka)